JOURNAL OF GEOPHYSICAL RESEARCH, VOL. 116, D23104, doi:10.1029/2011JD016640, 2011

Genesis of Typhoon Nari (2001) from a mesoscale convective system

Da-Lin Zhang,[1,2] Liqing Tian,[2,3] and Ming-Jen Yang[2,4]

Received 28 July 2011; revised 12 September 2011; accepted 22 September 2011; published 2 December 2011.

[1] In this study, the origin and genesis of Typhoon Nari (2001) as well as its erratic looping track, are examined using large-scale analysis, satellite observations, and a 4 day nested, cloud-resolving simulation with the finest grid size of 1.33 km. Observational analysis reveals that Nari could be traced 5 days back to a diurnally varying mesoscale convective system with growing cyclonic vorticity and relative humidity in the lower troposphere and that it evolved from a mesoscale convective vortex (MCV) as moving over a warm ocean under the influence of a subtropical high, a weak westerly baroclinic disturbance, an approaching-and-departing Typhoon Danas to the east, and the Kuroshio Current. Results show that the model reproduces the genesis, final intensity, looping track, and the general convective activity of Nari during the 4 day period. It also captures two deep subvortices at the eye-eyewall interface that are similar to those previously observed, a few spiral rainbands, and a midget storm size associated with Nari's relatively dry and stable environment. We find that (1) continuous convective overturning within the MCV stretches the low-level vorticity and moistens a deep mesoscale column that are both favorable for genesis; (2) Nari's genesis does not occur until after the passage of the baroclinic disturbance; (3) convective asymmetry induces a smaller-sized vortex circulation from the preexisting MCV; (4) the vortex-vortex interaction with Danas leads to Nari's looping track and temporal weakening; and (5) midlevel convergence associated with the subtropical high and Danas accounts for the generation of a nearly upright eyewall.

Citation: Zhang, D.-L., L. Tian, and M.-J. Yang (2011), Genesis of Typhoon Nari (2001) from a mesoscale convective system, *J. Geophys. Res.*, *116*, D23104, doi:10.1029/2011JD016640.

1. Introduction

[2] Tropical cyclogenesis (TCG) involves the growth of a preexisting atmospheric disturbance(s) into a self-sustaining, warm-cored moist vortex over a warm ocean through multiscale interactions, from the wind-induced surface heat exchange (WISHE) processes [*Emanuel*, 1986], to vortical hot towers (VHTs) [*Hendricks et al.*, 2004; *Montgomery et al.*, 2009] and larger-scale moisture convergence in the planetary boundary layer (PBL). Such a tropical disturbance(s) may be associated with easterly waves [*Ritchie and Holland*, 1999; *Molinari and Vollaro*, 2000], mesoscale convective systems (MCSs) or mesoscale convective vortices (MCVs) [*Zhang and Fritsch*, 1987; *Zhang and Bao*, 1996a, 1996b], monsoon trough gyres [*Landers*, 1994; *Harr et al.*, 1996], merger of MCVs [*Ritchie and Holland*, 1997; *Kieu and Zhang*, 2008], breakdown of the Intertropical Convergence Zone (ITCZ) [*Wang and Magnusdottir*, 2006; *Kieu and Zhang*, 2008], westerly wind bursts (WWBs) during the Madden-Julian Oscillation [*Lander*, 1990; *Hogsett and Zhang*, 2010], or just larger-scale flows [*Kurihara and Tuleya*, 1981]. Recently, *Dunkerton et al.* [2009] proposed the so-called "marsupial paradigm" for an easterly wave at whose critical layer a closed Lagrangian circulation is enhanced by diabatic heating and moistened by continuous convective overturning, and this circulation could become a "sweet spot" for TCG under favorable conditions. It appears that TCG is an extremely complex phenomenon with no single and distinct mechanism, depending on the origins of preexisting disturbances, larger-scale flows, sea surface temperature (SST), and certain interactive processes between them.

[3] Although several field experiments (e.g., the field campaigns of the Tropical Cloud Systems and Processes in 2005 [*Halverson et al.*, 2007]; the African Monsoon Multidisciplinary Activities in 2006 [*Zipser et al.*, 2009]; and the Pre-Depression Investigation of Cloud Systems in the Tropics Experiment [*Montgomery et al.*, 2011]) have provided much-needed high-resolution observations, they could only provide snapshots of certain mesoscale features associated with TCG. Much of our recent understanding of the mesoscale processes leading to TCG is based on a few limited

---

[1] College of Atmospheric Sciences, Nanjing University of Information Science and Technology, Nanjing, China.

[2] Department of Atmospheric and Oceanic Science, University of Maryland, College Park, Maryland, USA.

[3] Hebei Meteorological Observatory, Shijiazhuang, China.

[4] Department of Atmospheric Sciences, Institute of Hydrological and Oceanic Sciences, National Central University, Chung-Li, Taiwan.

0148-0227/11/2011JD016640

cloud-resolving studies of topical cyclones (TCs) using both idealized and real-data initial conditions. They may include the formation of Hurricane Diana (1984) from a cyclonic disturbance in a midlatitude frontal zone by *Hendricks et al.* [2004], TCG from idealized MCVs by *Montgomery et al.* [2006] and *Nolan* [2007], easterly waves [*Fang and Zhang*, 2010; *Wang et al.*, 2010], merging mesovortices associated with the ITCZ breakdowns [*Kieu and Zhang*, 2008], and thermodynamic transition of a tilted WWB vortex [*Hogsett and Zhang*, 2010]. In particular, MCSs/MCVs occur frequently over the vast tropical oceans, but only a few of them could develop into TCs, so our understanding of the mesoscale processes leading to developing TCs is far from complete. Clearly, more case studies are needed to investigate multiscale interactions involved in TCG, especially in association with MCSs/MCVs occurring in tropical near-barotropic flows.

[4] A number of observational and modeling studies have shown the development of MCVs in the stratiform region of MCSs in both tropical and midlatitude regions [e.g., *Leary and Rappaport*, 1987; *Zhang and Fritsch*, 1987, 1988; *Bartels and Maddox*, 1991; *Harr and Elsberry*, 1996]. MCVs may range from 50 to 300 km in radius with the vertical relative vorticity varying from 10^{-4} to 10^{-3} s^{-1} [*Zhang and Fritsch*, 1987; *Verlinde and Cotton*, 1990; *Zhang*, 1992; *Davis et al.*, 2004]. Their peak vorticity may occur at the melting level [*Ogura and Liou*, 1980; *Gamache and Houze*, 1982], or between 800 and 500 hPa [*Leary and Rappaport*, 1987; *Brandes*, 1990]. Some MCVs/MCSs have been observed to persist for several days, sometimes leading to TCG [*Bosart and Sanders*, 1981; *Harr and Elsberry*, 1996; *Zhang and Bao*, 1996a, 1996b]. In addition, recent cloud-resolving modeling studies allow us to see the development of VHTs with the sizes of 10–20 km in MCSs/MCVs [*Hendricks et al.*, 2004; *Montgomery et al.*, 2006, 2009]. They appear to play an important role in TCG through merging the associated vorticity anomalies and subsequent axisymmetrization processes. *Reasor et al.* [2005] provide observational evidence for the existence and interactions of VHTs in a developing TC. Clearly, the above studies reveal that convectively generated vortices of different scales are ubiquitous in MCSs and TCs. However, so far we have limited knowledge of their different roles in TCG.

[5] The objectives of this study are to (1) document TCG from a long-lived MCS and its subsequent intensity changes under a near-barotropic environment; (2) explore the multiscale interactions involved in the structural, track, and intensity changes during the genesis and subsequent intensification of a TC, and (3) examine the impact of a cold frontal passage on TCG and the generation of subvortices during the TC development. They will be achieved by analyzing the European Centre for Medium-Range Weather Forecasts (ECMWF) analyses, satellite observations, and mainly a 4 day (1200 UTC, 5 September to1200 UTC, 9 September) cloud-resolving simulation of Typhoon Nari (2001) with the finest horizontal grid size of 1.33 km. We are interested in this TCG case because (1) it originated from a tropical MCS moving on the southern and the southwestern periphery of a subtropical high; (2) it had a long life span of more than 20 days (i.e., between 0000 UTC, 1 September and 0000 UTC, 21 September 2001) starting from an MCS; and (3) it underwent erratic movements with two loops and variable structural and intensity changes over nearly the same ocean surface (i.e., a scale of about 500 km) during a 10 day period. In particular, none of the then-operational models predicted well the genesis, track, and intensity changes of the storm as well as its torrential rainfall over Taiwan and the Guangdong Province of mainland China. Because of its peculiar features, *Wu et al.* [2008] studied the effects of the air-sea interaction between Nari and the Kuroshio Current on its intensity changes during the period of 6–16 September. *Yang et al.* [2008] examined the role of topography in producing torrential rainfall after landfall over Taiwan island using a 108 h cloud-resolving simulation of Nari ending 0000 UTC, 19 September 2001, and *Yang et al.* [2011] further investigated the dynamic effects of Taiwan's high terrain on the generation of Nari's asymmetric structures of kinematics and precipitation features.

[6] The next section provides an overview of the large-scale environment in which Nari formed and traces its origin back to an MCS 5 days (i.e., 0000 UTC, 1 September) prior to its significant deepening using the ECMWF analysis and satellite observations. Section 3 describes the major model features used to simulate the development of Typhoon Nari (2001) from a weak depression. Section 4 provides verifications of the model-simulated track and intensity and other fields against a few available observations. Section 5 presents some mesoscale details during Nari's genesis that could not be seen from the synoptic analysis, especially the impact of a cold frontal passage on the genesis of the storm, and shows what mesoscale parameters or processes affect the size, track, and intensity of the storm. A summary and concluding remarks are given in the final section.

2. Overview

[7] Typhoon Nari (2001) first appeared as a tropical depression in the East China Sea, at about 250 km to the east of Taiwan, at 0000 UTC, 6 September 2001, at which time its best track, issued by the Joint Typhoon Warning Center (JTWC), began (Figure 1a). An examination of satellite imagery and ECMWF's analysis indicates that Nari's origin could be traced back to 5 days earlier, i.e., 0000 UTC, 1 September, to a tropical disturbance collocated with an organized MCS at about 800 km farther to the south, i.e., just off the east coast of the Philippines (i.e., 15°N, 130°E) (Figures 2a and 3). This tropical disturbance moved northwestward first, and then northward and northeastward under the influence of a subtropical high, mostly of the mean flow in the lower half of the troposphere (Figure 4a). This high was later separated from its major high-pressure system to the east and weakened soon after the intrusion of an intense typhoon, i.e., Danas, that was moving northwestward toward central Japan (Figures 1a and 2). A quasi-stationary low, situated over the Gulf of Tonkin (Figures 2c–2f), induced a low-level jet feeding the tropical warm and moist air into Nari's genesis region.

[8] More importantly, the pre-Nari disturbance moved along and to the east of the western boundary oceanic current (near 30°C; see Figure 1a) and then along the southern edge of the Kuroshio Current [*Wu et al.*, 2008], which would clearly provide necessary sensible and latent heat fluxes for

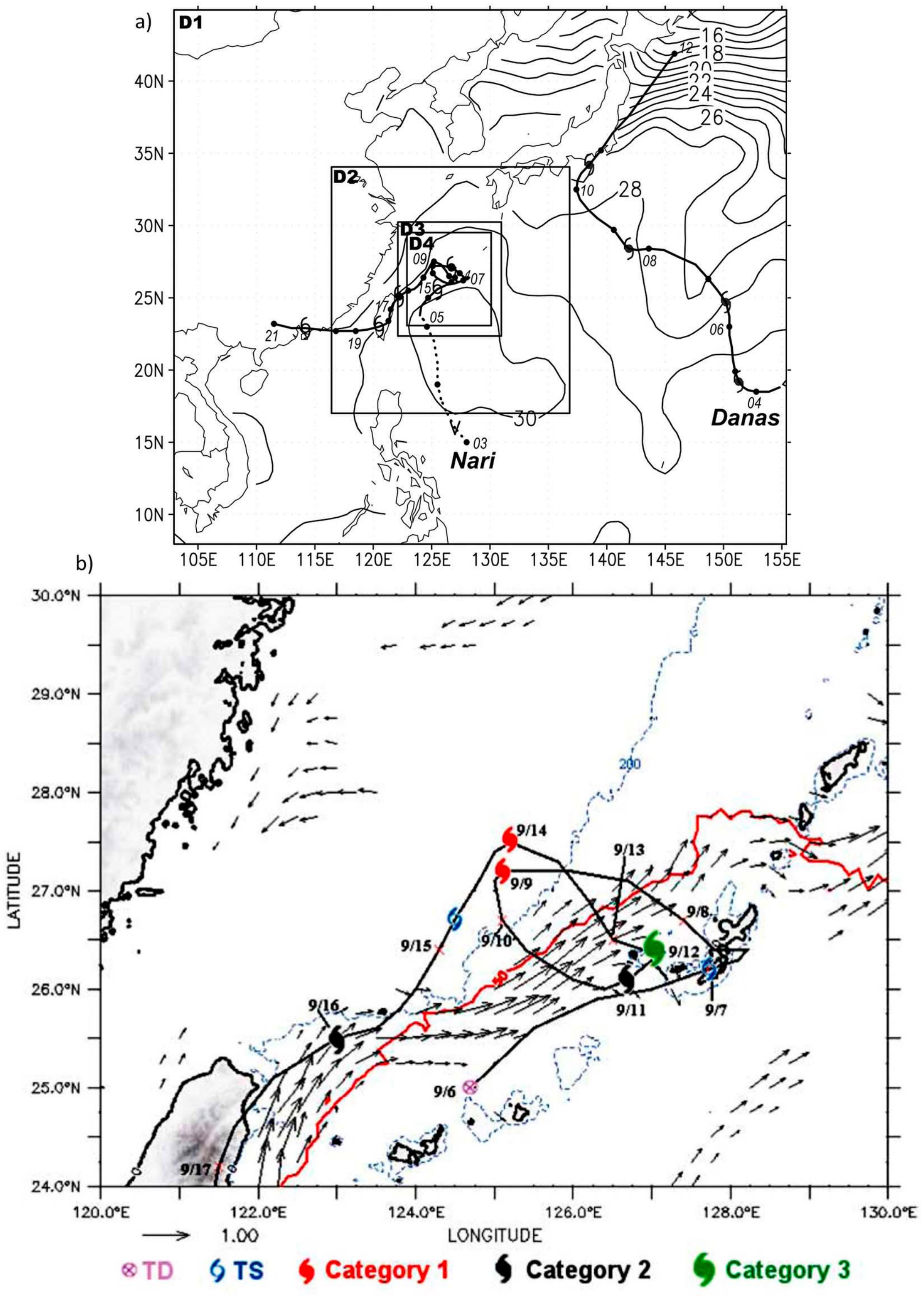

Figure 1. (a) The nested-grid domains used for the simulation (i.e., D1, D2, D3, and D4 with horizontal resolutions of 36, 12, 4, and 1.333 km, respectively), superimposed by the weekly mean SST (solid) at intervals of 1°C during the period of 2–8 September 2001, and the best tracks of Typhoons Nari (6–21 September) and Danas (4–12 September) during their life cycles. Dashed lines are used to reveal the origin of the pre-Nari disturbance. (b) Track and intensity of Nari (thick solid line) and the simulated Kuroshio flow vectors, which are taken from *Wu et al.* [2008].

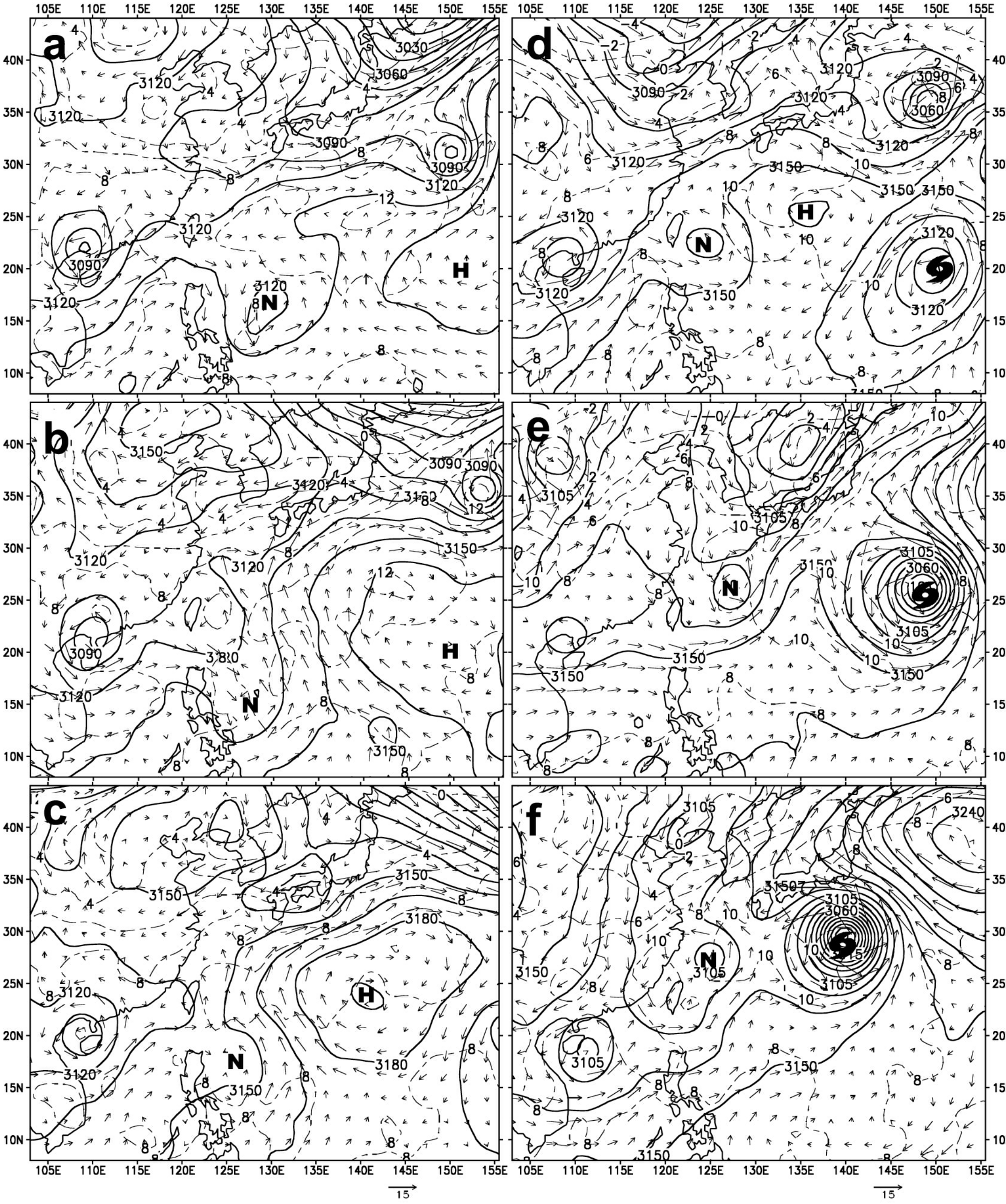

Figure 2. Horizontal distribution of 700 hPa height (solid, every 15 m), temperature (dashed, every 2°C), and horizontal wind vectors (m s^{-1}) from the ECMWF analysis at (a) 0000 UTC, 1 September; (b) 0000 UTC, 2 September; (c) 0000 UTC, 3 September; (d) 0000 UTC, 5 September; (e) 0000 UTC, 7 September; and (f) 0000 UTC, 9 September 2001. The symbol "N" denotes the low-level vorticity center of Nari, "H" denotes the local high pressure, and Danas is indicated by a typhoon symbol.

convective development during the course of Nari's genesis. For the convenience of the reader, Nari's track and intensity with respect to the simulated Kuroshio Current, taken from *Wu et al.* [2008], are provided in Figure 1b.

[9] Figure 3 (left) shows that the MCS associated with the tropical disturbance, denoted by "C," expanded in cloud coverage at night (i.e., 2000–0800 local standard time (LST) or 1200–0000 UTC) and shrank during the daytime (i.e., 0800–2000 LST or 0000–1200 UTC), except for the period of 0600–1200 UTC, 5 September, during which time an opposite trend occurred. Such a diurnal characteristic of deep convection is similar to that found by many previous studies in which a daytime minimum and a nighttime maximum of satellite-observed cold cloud tops are favored over some tropical oceans as a result of the cloud-radiation interaction [e.g., *Gray and Jacobson*, 1977; *Janowiak et al.*, 1994]. One can also see from Figure 3 (left) that cold downdraft outflows appear to be responsible for the

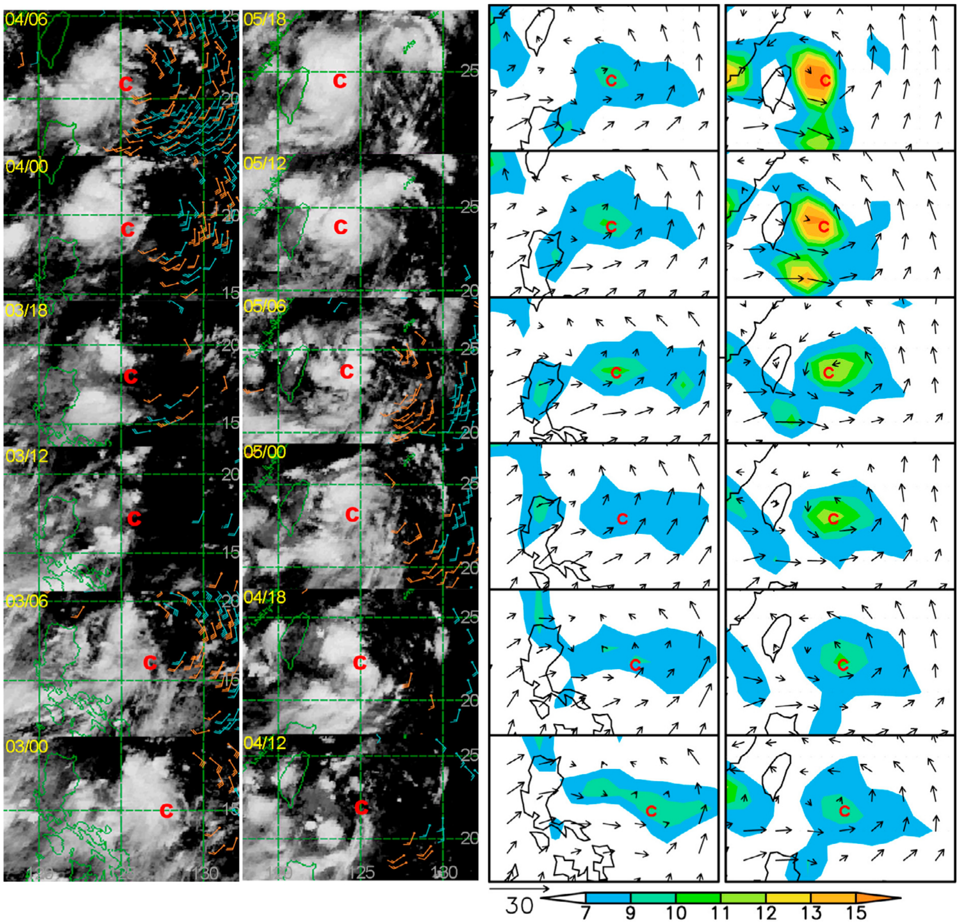

Figure 3. (left) The time evolution, at 6-hourly intervals, of satellite imagery and cloud-drifting winds (a full barb is 4 m s^{-1}) in the lower (i.e., 950–800 hPa, in green) and middle (i.e., 800–600 hPa, in orange) troposphere during the period of 0000 UTC, 3 September to1800 UTC, 5 September 2001. (right) The same as Figure 3 (left) except for the 850 hPa absolute vorticity (10^{-5} s^{-1}) and horizontal wind vectors (m s^{-1}) from the ECMWF analysis. The letter "C" is used to denote the vorticity center taken from panels in Figure 3 (right).

dissipation of deep convection before the daytime began; they are more visible to the east or north of the MCS (e.g., at 1400 UTC, 2 September, 1200 UTC, 3 and 4 September) likely because of the presence of the dominant midlevel dry air associated with the subtropical high. Of interest is that a deep layer of the concentrated vertical relative vorticity with its peak value at 850 hPa, based on the ECMWF analysis and supported by a mesoscale vortex circulation visible from the cloud-tracking satellite winds in the 800–600 hPa layer, remained over the wake region of the MCS until 1200 UTC, 4 September (Figure 3, left), and then it was shifted into the central portion of the MCS. Meanwhile, its peak magnitude was increased by more than 50%, to a value of 1.5×10^{-4} s^{-1} at 1800 UTC, 5 September (Figure 3, right), and it may be considered as an MCV with a closed circulation size of about 250–300 km in radius [*Zhang and Fritsch*, 1987]. Clearly, this MCV was intensified as a result of latent heat release in the MCS, which was more efficient when both the MCV and MCS were collocated, i.e., because of the stretching of the existing absolute vorticity [*Zhang and Fritsch*, 1987, 1988].

[10] Despite several days of continuous convective overturning, the prestorm environment was still unfavorable for TCG prior to September 5. Figure 4b shows that this was attributable to the presence of a strong vertical wind shear (VWS), which was as large as 14 m s^{-1} (estimated between 200 and 850 hPa) and the drying of the lower half of the troposphere by moist downdrafts. According to *Kieu and Zhang* [2008] and *Tang and Emanuel* [2010], these two factors are correlated because the thermodynamic impact of VWS is to ventilate the midlevel low-θ_e (equivalent potential temperature) air downward through moist downdrafts, thereby cooling and drying the lower troposphere. As the VWS decreased later to less than 6 m s^{-1}, convective overturning began to more effectively moisten the vertical columns, raising the storm-scale relative humidity (RH) to more than 90% near the top of the PBL and 80% up to 400 hPa shortly after 0000 UTC, 5 September (Figure 4a). Such a high RH and low VWS are considered as favorable conditions for TCG [*Nolan*, 2007]. In fact, the pre-Nari disturbance did begin to intensify after 1200 UTC, 5 September, given a warm ocean surface and the increased low-level cyclonic vorticity. However, as will be shown in section 5, the

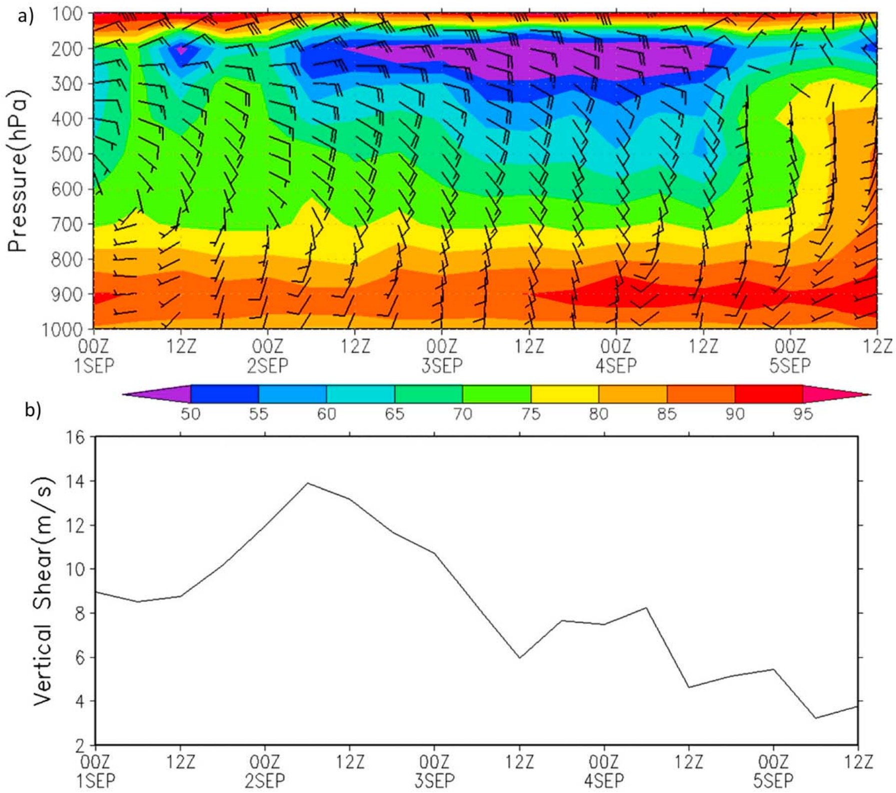

Figure 4. (a) Time-height cross section of the area-averaged horizontal winds (a full barb is 4 m s^{-1}) and relative humidity (percent, shaded) and (b) time series of the area-averaged vertical wind shear (m s^{-1}) between 200 and 850 hPa, which are obtained over an area of 1000 km × 1000 km centered at the surface circulation from the ECMWF analysis.

passage of a weak cold front, associated with a propagating midlevel trough in the midlatitude westerlies (Figures 2d and 2e), interrupted the otherwise continued deepening of the system by altering convective organization around its circulation during the period of 2100 UTC, 5 September through1200 UTC, 6 September 2001 (Figures 5 and 6).

[11] Satellite imagery shows the reorganization of deep convection in the MCS near 1500 UTC, 6 September (not shown), which quickly upgraded the MCV to tropical storm intensity at 1800 UTC, 6 September (Figure 6), as it moved northeastward at a speed of 4.5 m s^{-1}. This could also be seen from the more circular, robust cloud shields in Figure 5. The storm continued to intensify at an average rate of 0.5 hPa h^{-1}, until 1800 UTC, 7 September, when its deepening rate began to decrease and subsequently weakened after arriving at Okinawa Island at 0000 UTC, 8 September (Figures 1b and 6). This appears to be attributable partly to the upwelling of colder water and partly to the island's frictional effects for such a small storm, when considering the fact that it had been quasi stationary for about 24 h near the island after 0000 UTC, 7 September. This quasi-stationary character seems to be consistent with the presence of weak flows in Nari's environment (Figures 2e and 2f). As will be shown in section 5, the midlevel dry intrusion of continental dry air mass also appears to contribute to the weakening of the storm.

[12] Subsequently, Nari circled slowly (i.e., at a speed of about 2 m s^{-1}) for 7 days within a radius of 150 km near 126°E, 26°N (Figures 1a, 2, and 5h), resulting from the influence of Typhoon Danas passing by at about 700–1000 km to the east, as will be shown in section 4. Note how compact Nari's circulation size, like a midget storm, as compared with that of Danas or the other typical tropical storms (cf. Figures 2e, 2f, and 5h). As Nari left Okinawa Island and moved northwestward across the Kuroshio Current (Figure 1b), it began to intensify and reached typhoon intensity (37 m s^{-1}) at 0000 UTC, 8 September, with an eye at 0000 UTC, 9 September (Figures 5h and 6). Based on the JTWC best track analysis, Nari underwent a weakening stage (from 0600 UTC, 9 September to 1200 UTC, 10 September, with the peak winds decreased from 38 to 33 m s^{-1}) as it moved over a shelf and slope region with colder water to the north of the Kuroshio; a second major intensifying stage (from 1200 UTC, 10 September to 1200 UTC, 11 September, with the peak winds increased to 52 m s^{-1}) as it traversed southeastward over the Kuroshio; and a second major weakening stage (from 1200 UTC, 11 September to 0600 UTC, 13 September, with the peak winds decreased below typhoon intensity) after turning northwestward over nearly the same ocean surface as it had meandered earlier (Figure 1b). On 14 September, Nari redeepened to typhoon intensity (from 31 to 47 m s^{-1}) after turning southwest toward Taiwan Island and leaving the ocean surface on which it had stayed. On the evening of 16 September, it brought record-breaking rainfall (i.e., over 1000 mm in 24 h) and strong winds to Taiwan as it interacted with local

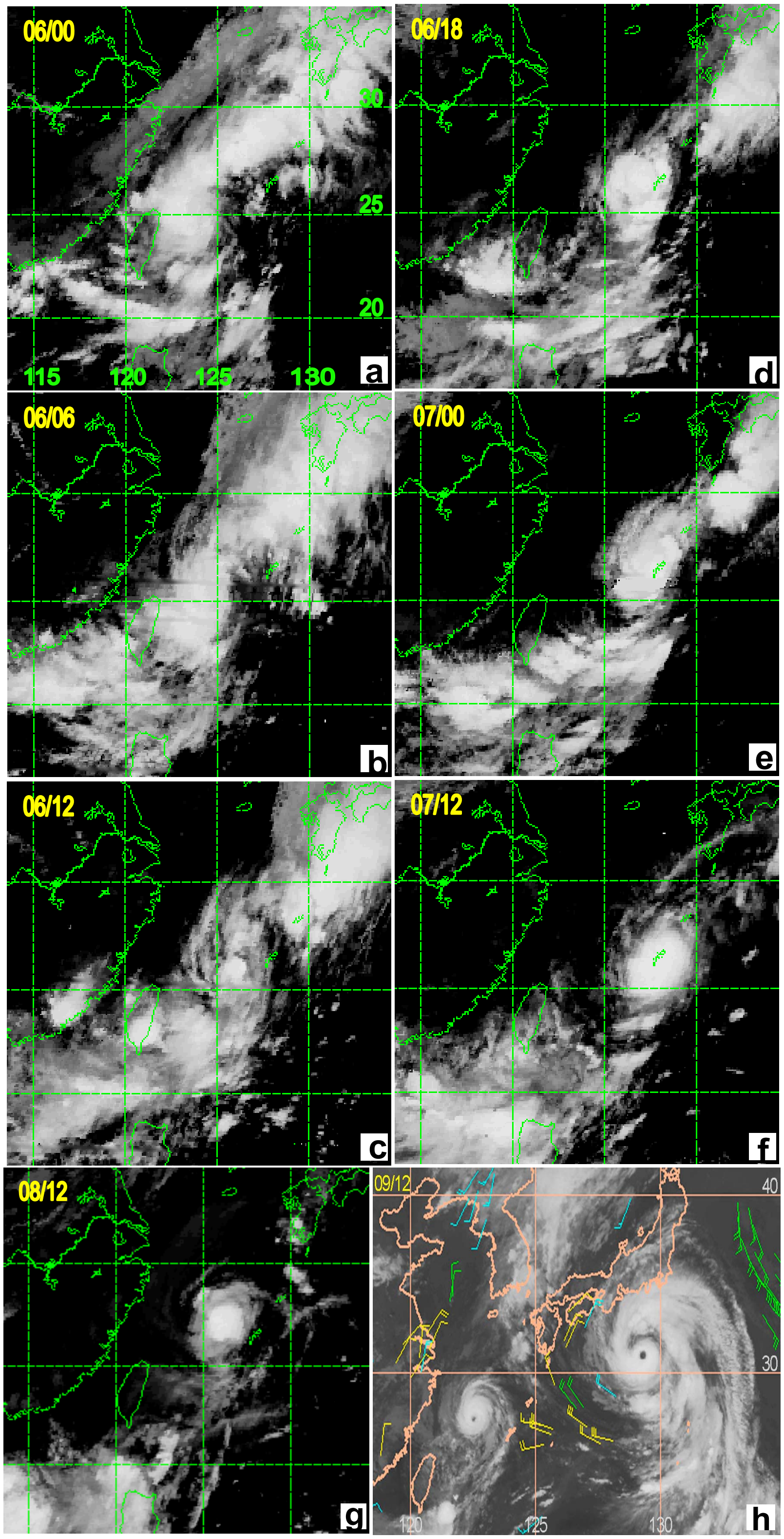

Figure 5. Satellite imageries at some selected times: (a) 0000 UTC, 6 September; (b) 0600 UTC, 6 September; (c) 1200 UTC, 6 September; (d) 1800 UTC, 6 September; (e) 0000 UTC, 7 September; (f) 1200 UTC, 7 September; (g) 1200 UTC, 8 September; and (h) 1200 UTC, 9 September 2001.

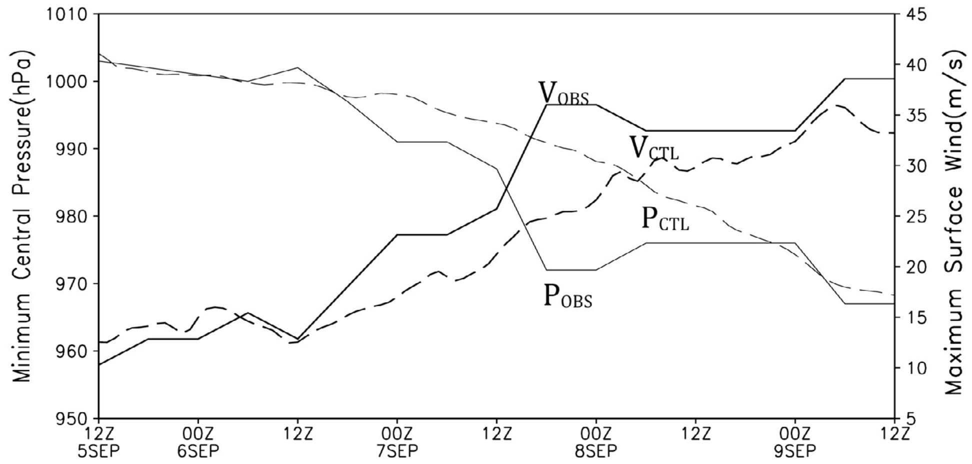

Figure 6. Time series of the minimum sea level pressure (P_{OBS}, P_{CTL}) and the maximum surface wind (V_{OBS}, V_{CTL}) from the best track (solid, OBS) and simulated (dashed, CTL from D2) for Typhoon Nari during the period of 1200 UTC, 5 September to 1200 UTC, 9 September 2001.

topography [*Yang et al.*, 2008]. Nari moved rapidly and experienced its fourth intensification after entering the Taiwan Strait on 19 September. It entered the Guangdong Province of mainland China on the following day and then quickly dissipated on 21 September (Figure 1a). While the air-sea interaction of *Wu et al.* [2008] appears to explain several intensity changes of Nari, we will show from the model simulation in section 5 that some atmospheric processes could also make important contributions, at least during our study period.

[13] In summary, Nari developed from an MCS/MCV and underwent variable intensity changes with a complicated track and a long history of about 21 days. Its size was much smaller than a typical TC, and its initial environment was characterized by anomalously warm SST, a mesoscale moist column after several days of convective overturning, a midlevel trough superimposed on a split subtropical high, a quasi-stationary low over the Gulf of Tonkin, the approach of Typhoon Danas, and traveling disturbances in the midlatitude westerlies. In the next few sections, we focus more on the genesis and intensification of Nari from a weak depression to a typhoon during a 4 day period. We wish to examine to what extent a mesoscale model could reproduce Nari's genesis in a near-barotropic environment and its complicated track using the ECMWF analysis as the model initial conditions. Then, the model output is used to investigate some nonobservable features and explore why Nari was midget-sized with few spiral rainbands and what atmospheric processes account for its genesis from an MCS.

3. Model Description

[14] In this study, a two-way interactive, quadruply nested-grid (36/12/4/1.333 km), nonhydrostatic (V3.6) version of the Penn State University-National Center for Atmospheric Research (PSU-NCAR) model (i.e., MM5) [see *Zhang et al.*, 1986; *Dudhia*, 1993] is used to simulate Nari's genesis with the finest grid size of 1.333 km (see Figure 1 for the nested domains). A large oceanic area to the east is included for the outermost domain in order to simulate the intensity of Typhoon Danas (2001) and its steering effects on the track of Nari (Figure 2). In fact, we have noted *large errors in Nari's track* during our initial experimentation (not shown) when Danas' evolution was partly specified through the lateral boundary conditions with a smaller domain to the east. The (x, y) dimensions of the outermost (D1) to the innermost (D4) domains are 163 × 133, 190 × 178, 247 × 247, and 601 × 601, respectively; they are overlaid on the Mercator map projection. Note that because of the programming limitations in adapting the MM5′s movable procedures to our Linux computer cluster, the finest-mesh domain is fixed with time. There are 43 uneven σ levels or 42 σ layers for all grid meshes with higher resolutions in the PBL and top layers. The 43 σ levels are placed at the values of 1.0, 0.996, 0.99, 0.982, 0.972, 0.96, 0.945, 0.925, 0.9, 0.87, 0.84, 0.81, 0.78, 0.75, 0.72, 0.69, 0.66, 0.63, 0.6, 0.57, 0.54, 0.51, 0.48, 0.45, 0.42, 0.39, 0.36, 0.33, 0.3, 0.27, 0.24, 0.21, 0.18, 0.15, 0.12, 0.09, 0.07, 0.05, 0.03, 0.02, 0.01, 0.005, 0. The model top (p_t) is defined at 50 hPa and the half-σ surface layer is placed roughly at $z = 15$ m.

[15] The model physics used for the outermost two domains (i.e., D1 and D2) include the most recent version of the Kain-Fritsch cumulus parameterization [*Kain*, 2004], the Blackadar PBL scheme [*Zhang and Anthes*, 1982], and a cloud-radiation interaction scheme. For the 4 and 1.333 km grid-size domains, the model water cycle is simulated with the cloud microphysics scheme of *Tao and Simpson* [1993], in which a three-class ice scheme is included, and no cumulus parameterization scheme is used; see Table 1 for more details. All the physics schemes are similar to those used by *Liu et al.* [1997] and *Zhu et al.* [2004].

[16] The MM5 is initialized at 1200 UTC, 5 September 2001, which is 12 h prior to the beginning of the best track and 24 h before the occurrence of notable intensification, using the ECMWF's 1.25° resolution analysis as the first guess that is enhanced by upper air and surface observations. However, the upper air sounding in the northern Taiwan is not used in the enhanced analysis because it was taken in a localized cloud system with a small dew point depression; this near-saturated condition did not appear to be

Table 1. The Model Design

Parameter	Domain D1	Domain D2	Domain D3	Domain D4
Dimensions (*x*, *y*)	163 × 133	178 × 190	247 × 247	601 × 601
Area (km^2)	5832 × 4752	2124 × 2268	984 × 984	800 × 800
Grid size (km)	36	12	4	1.333
Time step (s)	90	30	10	3.33
Integration hours	0–96	0–96	12–96	12–96
Implicit scheme	Kain-Fritsch	Kain-Fritsch	No	No
Explicit scheme	Tao-Simpson	Tao-Simpson	Tao-Simpson	Tao-Simpson
PBL	Blackadar	Blackadar	Blackadar	Blackadar

representative for the nearby mesoscale environment. We found that including this sounding tends to produce fictitious convective storms during the first few hours of integration (not shown). The model is then integrated for 96 h ending 1200 UTC, 9 September 2001. No bogus TC data are incorporated into the model initial conditions, including Danas' vortex. The SST field is updated, following *Zhu et al.* [2004], every 12 h in accordance with the Tropical Rainfall Measuring Mission (TRMM) Microwave Imager (TMI) satellite observations. Any data that is missing because of heavy rainfall contaminations over the storm area are filled by interpolation in both time and space. Nevertheless, the Kuroshio effects on Nari's development, as discussed by *Wu et al.* [2008], could not be seen from the TMI data because of the combined rainfall contamination and Nari's slow movement. Only slight localized cooling (i.e., 0.2°C–0.3°C) in the vicinity of Nari's track could be noted after the first 48 h integration.

[17] Because of the needed model moisture spin-up from the coarse-resolution initial conditions, the outermost two domains (i.e., D1 and D2), in which the Kain-Fritsch scheme is incorporated, are first integrated for 12 h, and the innermost two domains (i.e., D3 and D4) are then activated by interpolating from their mother domain. It should be mentioned that this procedure of using a convective parameterization during the first 12 h integration is necessary in order to help trigger grid-box saturation within the initial depression circulation in D3 and D4. Most of the figures shown herein will be plotted from the D4 simulation, unless mentioned otherwise. The lateral boundary conditions for the outermost domain are interpolated in time from the 12 hourly ECMWF analyses. Table 1 provides a more detailed description of the model initialization and integration procedures.

4. Model Verification

[18] The larger-scale environment in the model initial conditions is characterized by a marginally closed circulation at 900 hPa, an elongated zone of warmer air (>22°C) with higher absolute angular momentum (AAM) outside the radius of 400–500 km to the south and east and a weak baroclinic zone approaching Nari's vortex from the northwest (Figure 7). (Note that a tropical depression, if plotted at 2 hPa intervals, could not be defined at this time.) The higher AAM is dynamically consistent with the higher pressure gradients that result from superimposition of the depression on the split subtropical high (Figure 2d). This warm westerly airstream coincides with the underlying warm Kuroshio Current (Figure 1b) and provides the necessary convective available potential energy (CAPE) for deep convection leading to the subsequent genesis of Nari. A mesoscale moist column with the mean relative humidity of 80%~90% occurs over Nari's central area (Figures 4a and 8a) as a result of continuous convective overturning, as mentioned before.

[19] Before examining the detailed structures and evolution of the simulated Nari, it is necessary to make sure that the model could reproduce some observed fields of the storm. For this purpose, we compare first the time series of the simulated storm intensity and track from D2 with the best track analysis in Figures 6 and 7, respectively. Despite the use of the ECMWF synoptic-scale analysis as the initial conditions, the model appears to reproduce reasonably well the first 4 day complicated track of the storm shown in Figure 1, including its initial northeastward movement, a sharp westward and northwestward turn at 48 h into the integration, valid at 1200 UTC, 7 September (hereafter 7/12–48), and the beginning of a southward turn near the end of the 96 h integration (Figure 7). The maximum position error is about 80 km. The model also reproduces reasonably well the general intensity changes and final intensity in terms of the minimum sea level pressure and the maximum surface winds, including the slight weakening of the storm near 9/12–96 which is due to the previously mentioned weak cooling in the SST. Moreover, the model captures well the first 36 h slow formation stage, associated with the passage of the baroclinic disturbance, during which period the simulated Nari deepens only by about 3–4 hPa.

[20] Of course, there are several shortcomings with the simulation. For example, the model underpredicts the storm intensity during the period of 7/12–48 to 8/06–66 when Nari

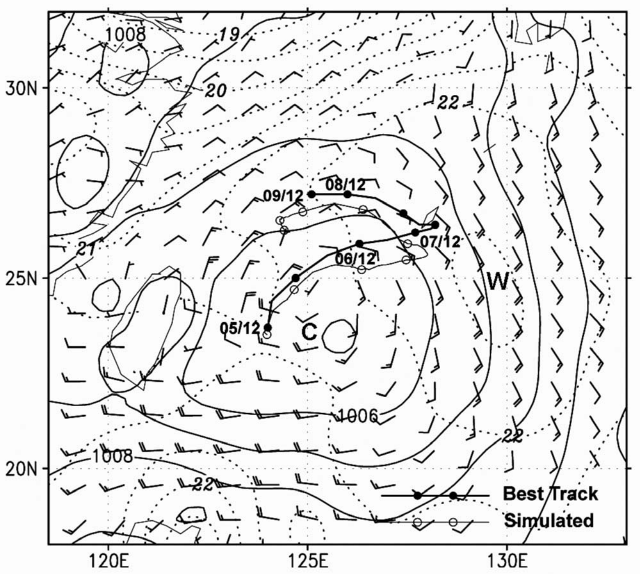

Figure 7. Horizontal distribution of surface winds (a full barb is 5 m s^{-1}), superimposed with the sea level pressure (solid, every 1 hPa) and 900 hPa temperature (dashed, every 0.5°C), at the model initial time (i.e., 1200 UTC, 5 September 2001). The best (open circles) and simulated (solid circles) tracks at 12 h intervals are also shown. The letters "C" and "W" denote the cold and warm centers, respectively.

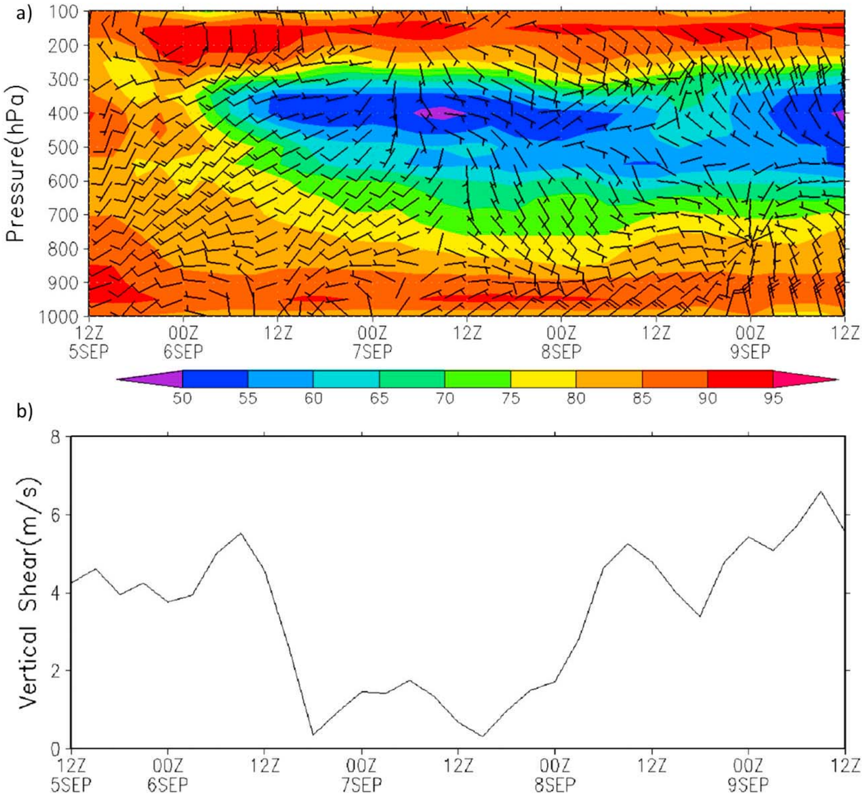

Figure 8. As in Figure 4 except from the 96 h simulation, valid between 1200 UTC, 5 September, and 1200 UTC, 9 September 2001.

moves across the Kuroshio [*Wu et al.*, 2008]; the peak difference is as large as 18 hPa or 15 m s^{-1} at 7/18/-54, although the localized intensity from D4, to be discussed in the next section, is 2–4 hPa stronger. This underprediction is attributable mainly to the lack of a realistic air-sea interaction with the Kuroshio, as mentioned before, and partly to the lack of mesoscale details (e.g., in moisture) over the vast ocean in the model initial conditions. On the other hand, note that, unlike over the Atlantic basin, the JTWC's best track analysis over the West Pacific is generally estimated from satellite data using the technique of *Dvorak* [1984], and it may also contain considerable uncertainties.

[21] To help understand the anomalous track of Nari, the time-height cross section of the area-averaged horizontal winds, given in Figure 8, shows that Nari's track, especially its abrupt turnings near 7/12–48 and 9/12–96, is determined by the larger-scale deep-layered flows. Specifically, Nari develops in a near-barotropic environment with weak VWS and weak horizontal flows, except for the passage of a weak cold front with a mesotrough aloft during the period of 5/12–00 to 6/12–24. The mean flow is about 6 m s^{-1} with a VWS of less than 2 m s^{-1} between 6/18–30 and 8/00–60, and about 4–6 m s^{-1} during the other periods. Of importance is that a pronounced decrease in VWS occurs after the complete passage of the baroclinic disturbance. Notwithstanding the small differences in the VWS, the weakest sheared environment appears to assist in the initial genesis of the storm, i.e., with more significant central pressure fall (cf. Figures 6 and 8). In this regard, the passage of the baroclinic disturbance only suppresses TCG temporally, and the TCG is resumed after the vortex circulation becomes reorganized (Figures 9 and 10), given the little-affected moist mesoscale column.

[22] Of further importance is that the mean winds are shifted sharply at 7/06–42 from southwesterly to a flow regime with easterly winds below and southeasterly winds aloft, as Danas approaches the same latitude as Nari (cf. Figures 8a and 2e). This easterly to southeasterly flow structure coincides with the sharp westward and northwestward turning of the track (cf. Figures 8a and 7). Another sharp wind shift, from northeasterly to northerly, occurs near 9/00–84, as Danas moves to the northeast of but closer to Nari, accounting for the southward turning of the track (cf. Figures 1b and 2f). Both sharp track turnings can be understood as the *Fujiwhara* [1921] effects associated with Typhoon Danas and can be examined through potential vorticity inversion following *Huo et al.* [1999]. The weak flow in the lower half of the troposphere also explains the quasi-stationary character of Nari during this period (cf. Figures 1 and 8a).

[23] Now let us compare the radar reflectivity, calculated following *Liu et al.* [1997], from the 15-h simulation (i.e., 6/03–15) to the satellite imagery at 0331 UTC, 6 September (Figure 9). During the first 12 h model integration, the parameterized convection in D2 is generated first in the westerly flow in the southern portion of the vortex and then

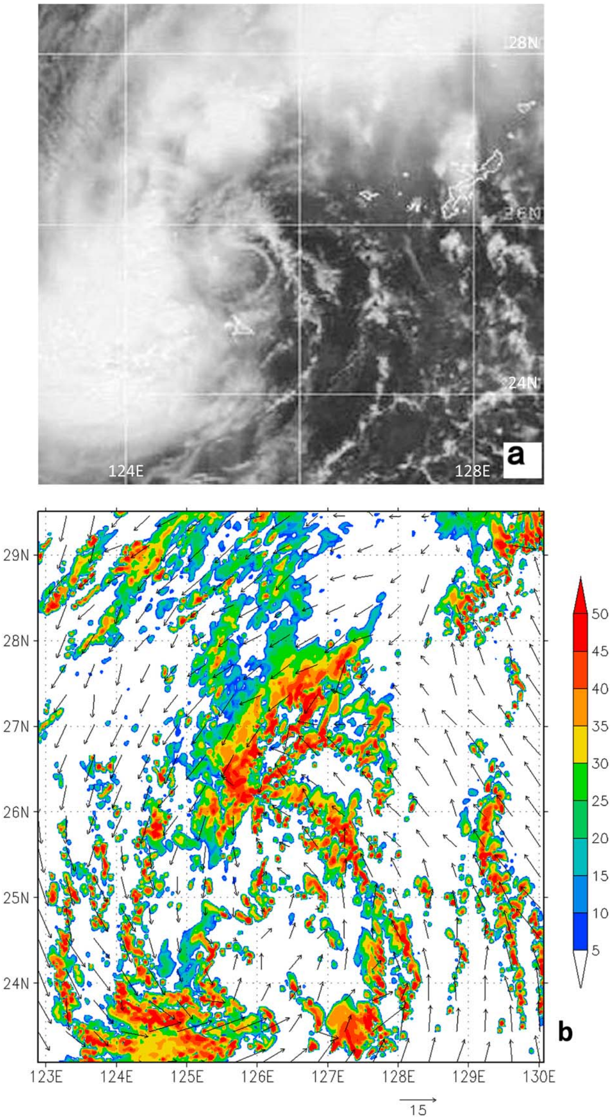

Figure 9. Comparison of (a) the satellite imagery at 0331 UTC, 6 September 2001, and (b) the 15 h simulated radar reflectivity at 900 hPa. The model-simulated surface wind vectors from the 15 h simulation are also superimposed.

along the weak baroclinic zone, but with few grid-resolved convective cells. It takes several hours for the model to spin up the grid-scale saturation as a result of the upward surface fluxes and moisture convergence in the PBL. In general, the model reproduces reasonably well the cyclonically distributed cloud streets over the areas where parameterized convection in D2 was previously active, although their widths appear to be larger than those observed because of the insufficient horizontal resolution and the lack of enough model spin-up time after the prognostic fields are interpolated from D2 to D4. It also reproduces the development of extensive deep convection ahead of the baroclinic zone to the north and circular cloud bands along the cyclonic warm airstream to the southwest. Little convection occurs near the vortex center because of little energy supply from the outer region and the presence of weak convergent flow (Figure 7).

[24] Although the above verifications are limited, we may state that the model initial conditions and physical parameterizations are reasonable based on the comparison of the cloud and rainfall fields (Figure 9), whereas the relatively small track errors of the simulated storm indicate indirectly that the evolution of larger-scale flows, especially the

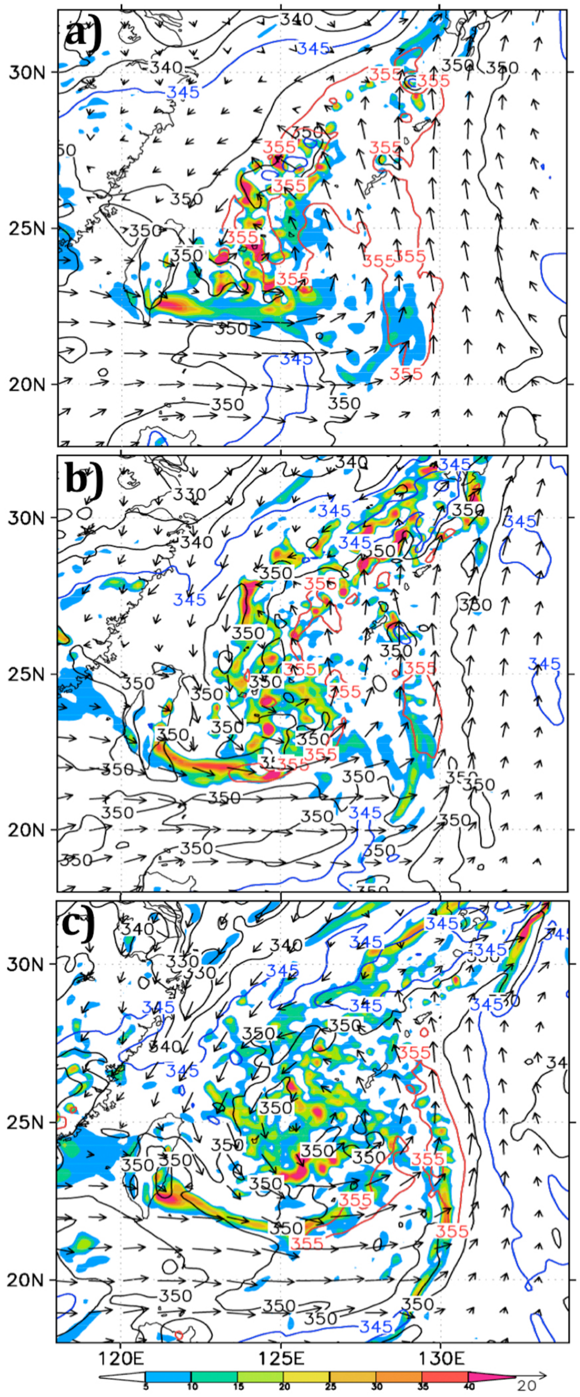

Figure 10. The simulated equivalent potential temperature (contoured at every 5 K, 355 K in red, and 345 K in blue), vertical relative vorticity (shaded), and horizontal flow vectors (m s^{-1}) at 900 hPa at (a) 05/18–06, (b) 06/00–12, (c) 06/06–18.

influence of Danas on Nari's track, is realistically simulated (cf. Figures 7 and 8).

5. Genesis From an MCS/MCV

[25] In this section, we use the model simulation to examine first the time evolution of the simulated Nari from an MCS to a compact-sized typhoon and then the genesis of Nari's rotational flows from a weak tropical depression.

5.1. From an MCS to a Compact Typhoon

[26] As mentioned in section 2, Nari's genesis was to a certain extent interrupted by the passage of a weak cold front. A comparison of Figures 7 and 10a shows the pronounced distortion of Nari's circulation and suppression of the preexisting convection within the MCS at 6 h into the simulation, starting from its northwest semicircle, as the front advances into the storm. As a result, the convectively generated cyclonic vorticity and deep convection (as indicated by lower-θ_e air associated with moist downdrafts) during the first 6–12 h are mostly concentrated along the southwest-northeast-oriented frontal zone; they are similar to the linearly organized convection seen in satellite imagery (cf. Figures 5 and 10). This frontal passage also reduces the size of vortex circulation, especially along the northwest-southeast direction (cf. Figures 7 and 10a). Nevertheless, because of its weaker and shallower forcing along the southern segment of the front, the relatively strong rotational flows in the southeastern semicircle are little influenced during this 12 h period (Figures 7 and 10a–10c). Thus, more organized convective activity takes place to the northeast where pronounced convergence occurs between the frontal zone and the warm southeasterly flow, and in the southern portion of the vortex where higher-θ_e air is present (Figure 10b). It appears to be this residue vortex that maintains nearly its prefrontal rotational intensity and high moisture content in the vertical column, and later gets reorganized, through axisymmetrization of the existing cyclonic vorticity [*Montgomery et al.*, 2006], after the passage of the cold front (Figures 10b and 10c). By 6/6–18, the MCV becomes fully recovered in terms of circulation size and shape and intensity in tangential flows, except to the northeast (Figure 10c). In addition, localized vorticity centers, corresponding to VHTs, are widespread in the core region and along several convective bands associated with the higher-θ_e air currents. Despite the recovery of the lower-level vortex circulation, both the model and observations do not show significant deepening of the storm until after 6/12–24 when the influence of the midlevel trough diminishes (cf. Figures 6, 8a, and 8b). Nari's central pressure has deepened only 5–6 hPa during the first 24 h. This slow deepening appears to be attributable partly to the passage of a midlevel trough, as mentioned before, and partly to the distribution of VHTs over the large region in the core.

[27] Figure 11 shows the subsequent evolution of the simulated surface and radar reflectivity fields over D4 until Nari reaches its full typhoon stage. The surface map at 6/12–24 shows tightened isobars and scattered deep convection over the core region, but with several distinct spiral bands (Figure 11a). With the supply of higher-θ_e air in the westerly flow to the south, the resulting increased vortex-scale convergence facilitates the further organization of deep convection. By 7/00–36, two elongated, arc-shaped rainbands are distributed in the north-to-northeasterly and south-to-southwesterly flows, denoted as B_1 and B_2, respectively, with continued convective activity in the warm, moist westerly flow (Figure 11b). Of importance is that the rainband B_1 begins spiraling into the vortex's core region from the south where lower pressures occur as a result of the more-organized deep convection. This spiral band appears to reveal why Nari could be contracted rapidly to a midget size from the preexisting vortex circulation of about 800 km in diameter (Figure 10c), as this spiral rainband will be shortly wrapped around to form an annular rainband that eventually evolves to an eyewall (see Figures 11b–11f). This spiral rainband can be traced back to an earlier convective band along the frontal zone, since it is nearly quasi stationary with respect to the vortex during the past 12 h (cf. Figures 10c, 11a, and 11b). This implies that such a midget TC size may be determined by larger-scale flows. In other words, without the frontal passage, Nari might begin with two symmetric arc-shaped rainbands at larger radii, and it may then take longer time for it to spin up to tropical storm intensity.

[28] By 7/12–48, both the inner (B_1) and outer (B_2) bands are wrapped around and then merged into an annular rainband as a result of axisymmetrization, with nearly a doubled width compared to the previous individual bands (Figure 11c). It is this annular rainband that is spun up, with increased radial pressure gradients, to form the eyewall (Figures 11c–11f). The core convective area is about 300 km in diameter compared with the original MCV size of about 800 km, which is close to that observed by the satellite (cf. Figures 11c and 5).

[29] Of particular interest is that the model produces two small-scale vortices with intense reflectivity nearby at the inner edge of the eyewall; the two subvortices last for more than 24 h (Figures 11c–11e). Initially they grow in size and intensity, but later they appear to be gradually absorbed by the mean TC vortex. (Note that their associated central pressures are not used in plotting Figure 6.) Similar subvortices have also been observed in Hurricane Dolly (1995) by *Reasor et al.* [2005, Figure 8], and at the eye-eyewall interface of Tropical Storm Gustav (2002) by *Hendricks and Montgomery* [2006, Figure 7a]. *Kossin et al.* [2002, Figure 2h] showed similar subvortical patterns in low-level cloud decks in the eyes of mature hurricanes. In fact, one of the examples was actually from Typhoon Nari (2001) at its later stage, but with three subvortices. Then, they used a nondivergent barotropic model to demonstrate that such subvortices occur as a result of the breakdown of the eyewall in the presence of barotropic instability. We have traced the origin of the subvortices back to 6/15–27 and earlier and found that they originate from mergers of smaller vortices (not shown). We speculate that the two subvortices might survive for a longer period if Nari's eye size were greater.

[30] Although the above phenomenon could not be verified by observations during this genesis stage due to the coverage of higher-level clouds, the previously demonstrated modeling capability of some small-scale features suggests that its structures and genesis mechanisms are worth studying. Thus, a vertical cross section taken through the centers of the two subvortices is given in Figure 12, which shows that both subvortices exhibit a deep layer of

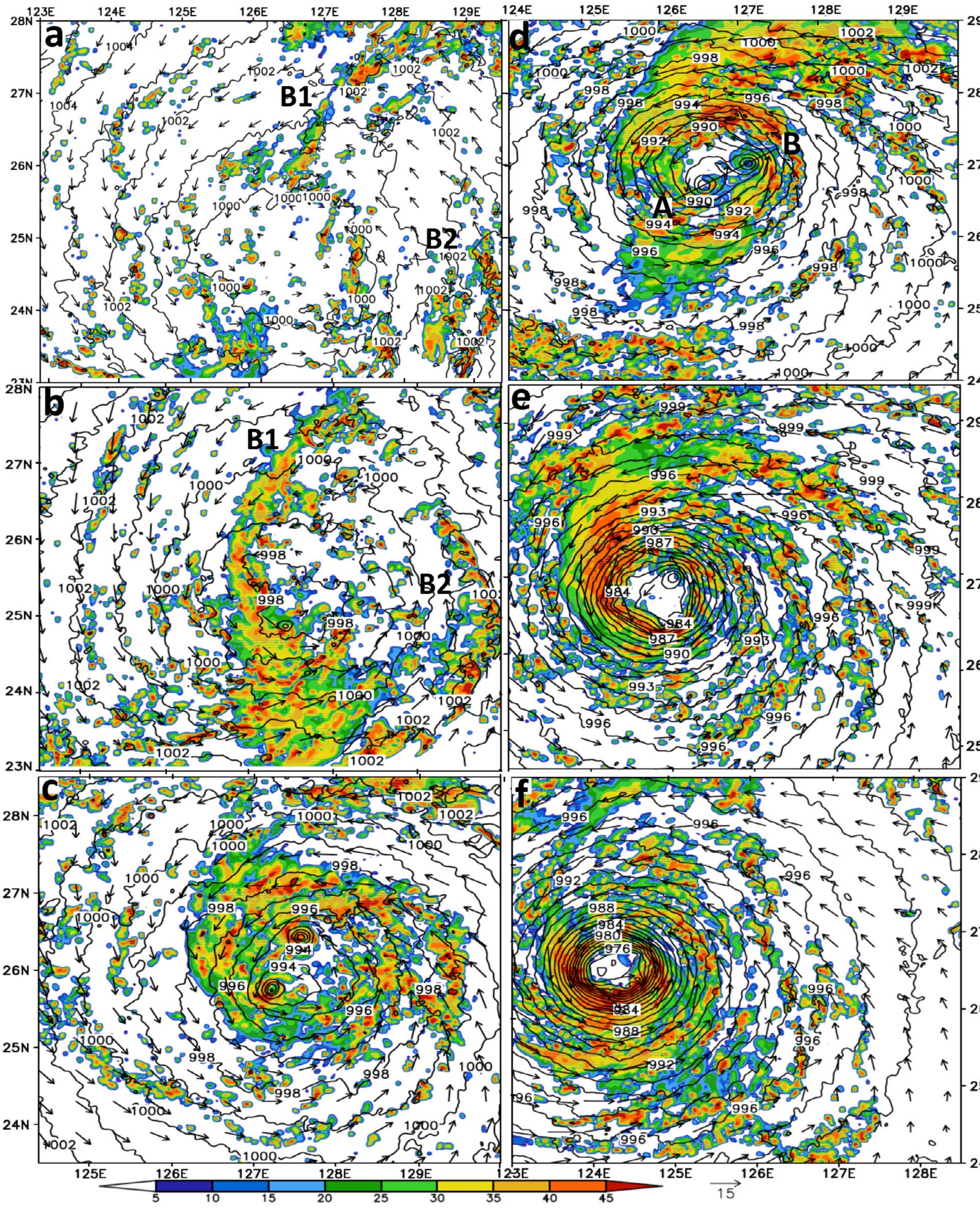

Figure 11. Horizontal distribution of the simulated radar reflectivity at 900 hPa (shaded), sea level pressure (solid, every 1 hPa), and surface wind vectors (m s^{-1}) at (a) 6/12–24, (b) 7/00–36, (c) 7/12–48, (d) 8/00–60, (e) 8/12–72, and (f) 9/00–84. Symbols b_1 and b_2 denote two major rainbands occurring during the genesis stage. Line A-B in Figure 11d is the location of the vertical cross section used in Figure 12.

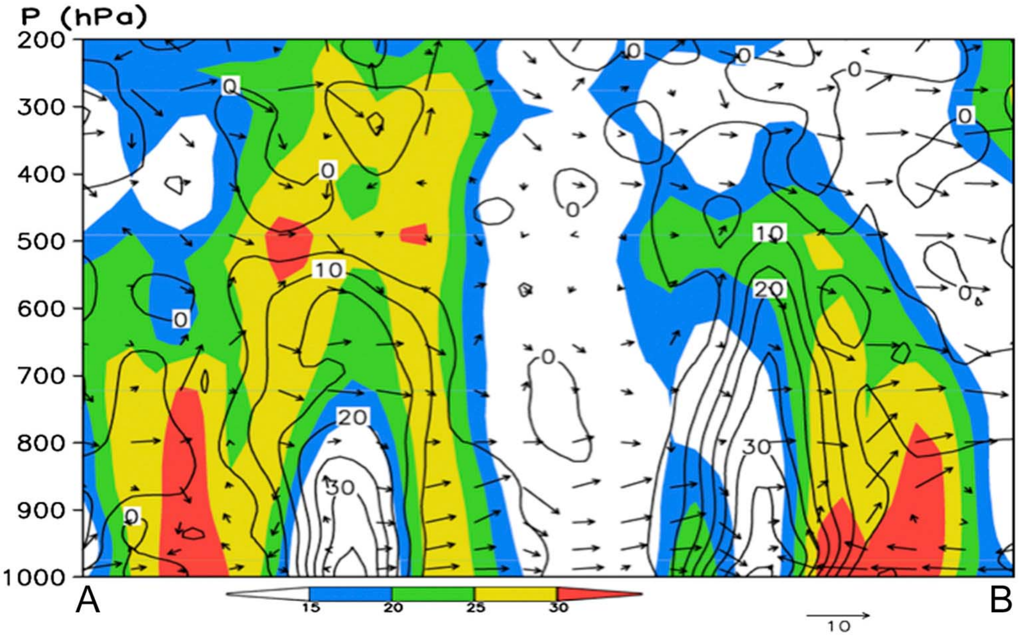

Figure 12. Vertical cross section of the simulated radar reflectivity (shaded), relative vorticity (solid, every 10^{-4} s^{-1}) and in-plane flow vectors (m s^{-1}) from the 60 h simulation along line AB (about 130 km) in Figure 11d. Vertical motion has been multiplied by 10.

cyclonic vorticity up to 500 hPa, with a maximum value of more than 4×10^{-3} s^{-1} in the lowest layer, and they have diameters of 30–35 km based on the relative vorticity of at least the local Coriolis parameter. The horizontal scale and intensity of these subvortices are close to those radar observed by *Reasor et al.* [2005] and satellite observed by *Hendricks and Montgomery* [2006]. Clearly, the subvortices contribute significantly to the intensification of the storm-scale rotation after eventually being merged into the eyewall, as also indicated by the above two observational case studies. It could also play an important role in transporting high-θ_e air from the eye into the eyewall, as mentioned by *Liu et al.* [1999]. Similarly, it transports cloudy air mass from the eyewall inward, thereby moistening the eye region, as indicated by weak rainfall in the eye (Figure 12).

[31] Of further interest is that the central portion of the subvortices is free of rainfall with little evidence of upward motion, but overhang by precipitating clouds from the eyewall. This indicates that evaporative cooling from the overhang clouds may account for the generation of the rain-free core, as could be seen from a few pronounced downward flow vectors aloft (Figure 12). This is consistent with the findings of *Liu et al.* [1997, 1999], who showed that a narrow but deep zone of penetrative downdrafts tends to occur at the eye-eyewall interface because of the evaporation of clouds and precipitation.

[32] It is also apparent from Figure 11 that the development of the two subvortices alters the shape of the eyewall from time to time, e.g., from a triangle at 7/12–48 to a square at 8/00–60, and a triangle again at 8/12–72, depending on their azimuthal propagation with respect to the locations of intense convection. These eyewall shapes are similar to the polygonal shapes discussed by *Schubert et al.* [1999], although the subvortices they studied are convectively generated in the eyewall rather than at its inner edge.

[33] Figure 11 also shows that as Nari intensifies, the annular rainband/eyewall size shrinks, e.g., by more than half between 7/12–48 and 9/00–84. Note that while the storm is intensifying, convective activity in the outer region decreases with time, especially in the west-to-southwesterly flows. The lack of the outer spiral rainbands is consistent with the small coverage of convective clouds seen from the satellite imagery and in significant contrast with the large area coverage of Danas (cf. Figures 5 and 11). A comparison of the CAPE between 6/12–24 and 9/12–96, as given in Figures 13a and 13b, indicates that the lack of outer rainbands can be attributed to the presence of decreasing CAPE in the outer region. That is, the initial high CAPE in the west-to-southwesterly flows decreases with time mainly because of the northeasterly advection of cold and dry air from the wake of Typhoon Danas and partly because of the upwelling of colder water [*Wu et al.*, 2008]. The storm-scale RH, given in Figure 8a, also shows the drying of the midtroposphere during this period, which may also account for the generation of such a midget-sized storm [*Hill and Lackmann*, 2009]. We see that in the western semicircle, the relatively colder and dry continental air mass is continuously fed into the prestorm environment by the northerly flows, and by 9/12–96 it has more or less wrapped around the storm and interrupted the west-to-southwesterly energy supply. This larger-scale influence could also be seen by comparing the 700-hPa θ_e maps between 6/12–24 and 9/12–96, as given in Figures 13c and 13d, which show clearly the intrusion of the continental lower-θ_e air into the vicinity of Nari through the northerly flow in the earlier stage and the westerly flows at the later stages. Ventilation of the midlevel lower-θ_e air facilitates the generation of moist downdrafts and suppression of deep convection in the outer region [*Kieu and Zhang*, 2008; *Tang and Emanuel*, 2010].

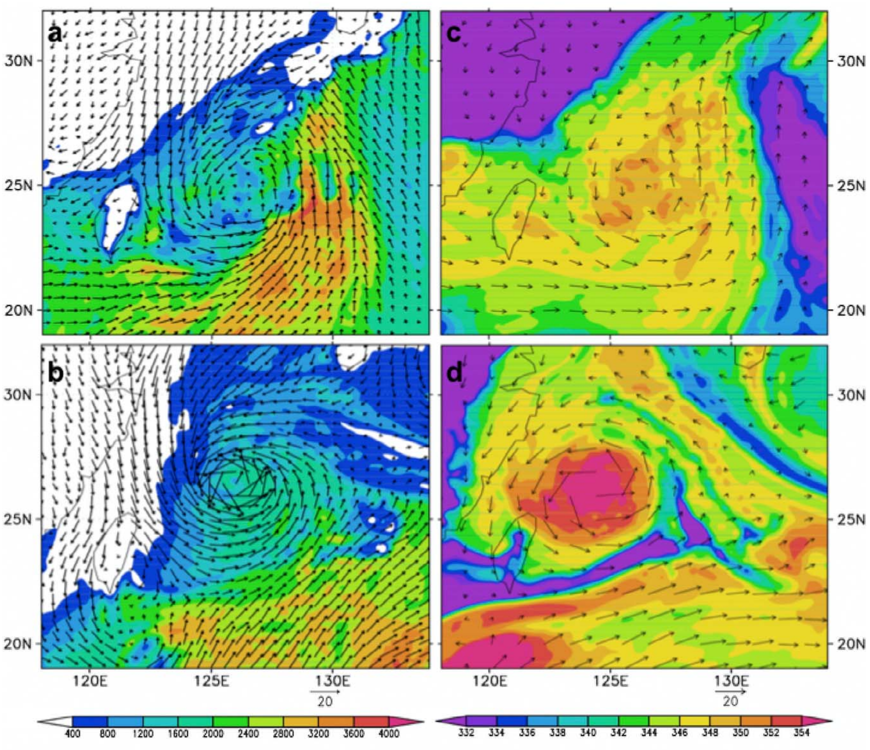

Figure 13. Horizontal distribution of (left) the maximum convective available potential energy superimposed with surface winds and (right) the equivalent potential temperature (θ_e) superimposed with 700 hPa flow vectors at (a and c) 6/12–24 and (b and d) 9/12–96.

[34] The decreasing CAPE and the wraparound of the midlevel lower-θ_e air in the outer region also appear to help explain partly why Nari began its slow weakening after 9/06–90 (Figure 6) and reached a steady state afterward as in the best track analysis until 1200 UTC, 10 September (not shown), as mentioned in section 2. Apparently, Nari's circling track, mainly because of the influence of Typhoon Danas, prevents it from accessing CAPE in its larger-scale environment until 14 September, when it moved southwestward away from the region (see Figure 1b). Thus, Nari's further growth is suppressed, given the limited energy sources from the narrow Kuroshio Current. These results indicate that both the air-sea interaction with the underlying Kuroshio Current and the overlying larger-scale environmental conditions could play important roles in regulating the storm size and determining Nari's multiple intensity changes, presumably including the second major deepening period of 0000 UTC, 10 September, to 1200 UTC, 11 September, as Nari moved southeastward across the Kuroshio again (see Figure 1b).

5.2. Spin-up of Nari's Rotational Flows

[35] As shown in Figures 3, 4a, and 8a, the formation of Nari occurs as its associated mesoscale column becomes sufficiently moist with the pronounced low-level to midlevel cyclonic rotation and weakened VWS. Figure 14 shows how the rotational flows are spun up in relation to convectively generated cyclonic vorticity in the eyewall during the subsequent intensifying stage. At 6/12–24, one can see two distinct layers of cyclonic vorticity that are greater than 3×10^{-4} s^{-1}: One is associated with a traveling midlevel trough in the 600–350 hPa layer with the southwesterly flow of greater than 18 m s^{-1} (Figure 14a) and the other in the lowest 300 hPa layer generated by the arc-shaped rainbands (cf. Figures 10c, 11a, and 14a). This pronounced midlevel vorticity results from the lateral flux convergence of absolute vorticity, as will be shown later, associated with the traveling trough into the MCV column, according to *Haynes and McIntyre* [1987] and *Kieu and Zhang* [2009], as indicated by the across-storm relative flows in the midtroposphere. It is evident from Figures 2d and 2e that the larger-scale environment exhibited relatively weaker flows after the passage of the midlevel trough. This is consistent with the reduced VWS, recovery of the vortex circulation, and the subsequent intensification of the storm at 6/12–24 (Figures 6, 8, 10, and 11a), indicating further the suppression and resumption of TCG during and after the passage of the baroclinic disturbance, respectively.

[36] After reaching tropical storm intensity at 7/12–48, a well-developed symmetric vertical circulation appears with converging flows in the PBL, ascending flows in the eyewall, outflows aloft, and weak subsidence in the eye (Figure 14b). Most of the midlevel vorticity and associated rotational flows seen earlier have been absorbed by the storm, forming a robust TC vortex with near-axisymmetric circulations up to 400 hPa (e.g., Figure 11c). Recall that this occurs in the presence of very weak VWS after the passage of the midlevel trough (Figures 9a and 9b). Meanwhile, the low-level cyclonic vorticity in the eyewall increases, e.g., to a peak value of 4×10^{-4} s^{-1}, as a result of the wraparound of the two rainbands (cf. Figures 11c and 14b). The vertical structures of the convectively generated vorticity in relation

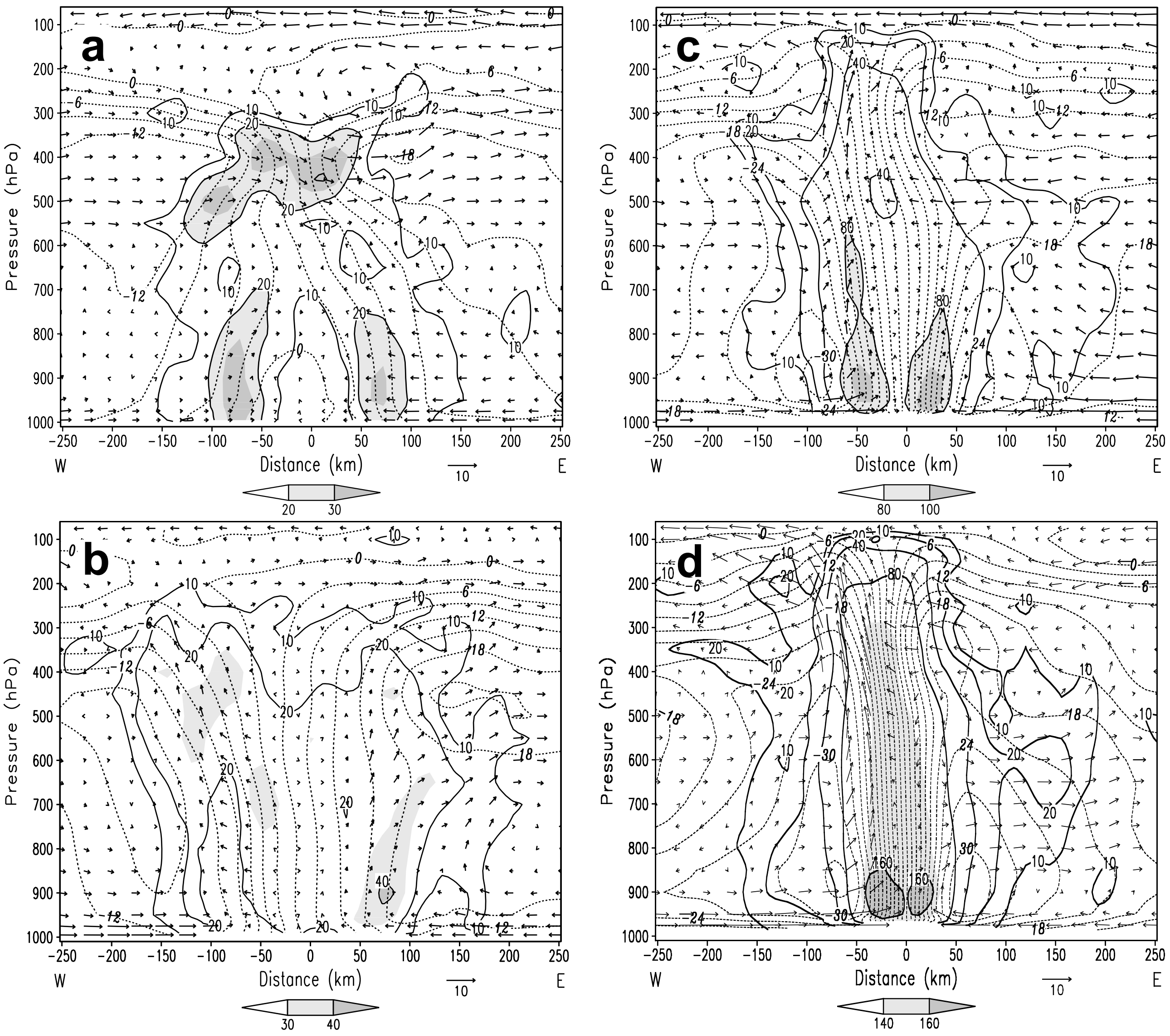

Figure 14. Vertical (west–east) cross section of the tangential wind (dotted, every 3 m s^{-1}), relative vorticity (solid, contoured at 10, 20, 40, 80 × 10^{-5} s^{-1}), and in-plane system-relative flow vectors (m s^{-1}) taken through the TC center from D2 at (a) 6/12–24, (b) 7/12–48, (c) 8/12–72, and (d) 9/12–96. Vertical motion has been multiplied by 10.

to the low-level to midlevel vortex resemble closely those shown by *Zhang and Bao* [1996b], in which TCG from an MCV results from the wraparound of the low-level cyclonic vorticity, albeit by parameterized deep convection.

[37] By 8/12–72, the peak cyclonic vorticity of greater than 10^{-3} s^{-1} takes place near the top of the PBL (Figure 14c), which is consistent with the findings of *Zhang and Bao* [1996b], *Hendricks et al.* [2004], and *Montgomery et al.* [2006] that TCG tends to occur from the bottom upward. Similarly, the maximum tangential wind shifts from 450 hPa downward to the lower levels as a result of converging the AAM in the PBL (cf. Figures 14a–14c and 15). Note that the midlevel tangential flows (i.e., at 500 hPa) also increase, e.g., from 12 to 15 to 24 m s^{-1} during the past 48 h (cf. Figures 14a and 14c), partly because of the contraction of the TC vortex and partly because of the presence of convergent sheared flows between the anticyclonic southwesterlies and east-to-northeasterlies associated with the subtropical high and northward-propagating Danas, respectively (cf. Figures 14c and 2e). For the same reason, the middle to upper level cyclonic vorticity amplifies substantially, since the divergence of vertically tilted horizontal vorticity [see *Kieu and Zhang*, 2009, equation (4)] is small in the eyewall where the vertical shear of tangential winds is relatively weak (Figures 14c and 14d). By the end of the 96-h simulation, the midlevel vorticity in the core region exceeds 1.4 × 10^{-3} s^{-1}, which is 4–5 times of that at 6/12–24 (cf. Figures 14a and 14d). Again, the peak vorticity with the maximum tangential winds of over 30 m s^{-1} appears near the top of the PBL.

[38] Of interest is that unlike the vertically tilted structures shown in the previously studies of hurricanes [e.g., *Liu et al.*, 1999; *Braun*, 2002; *Rogers et al.*, 2003; *Wu et al.*, 2006; *Yang et al.*, 2008, 2011], Nari's eyewall convection and the

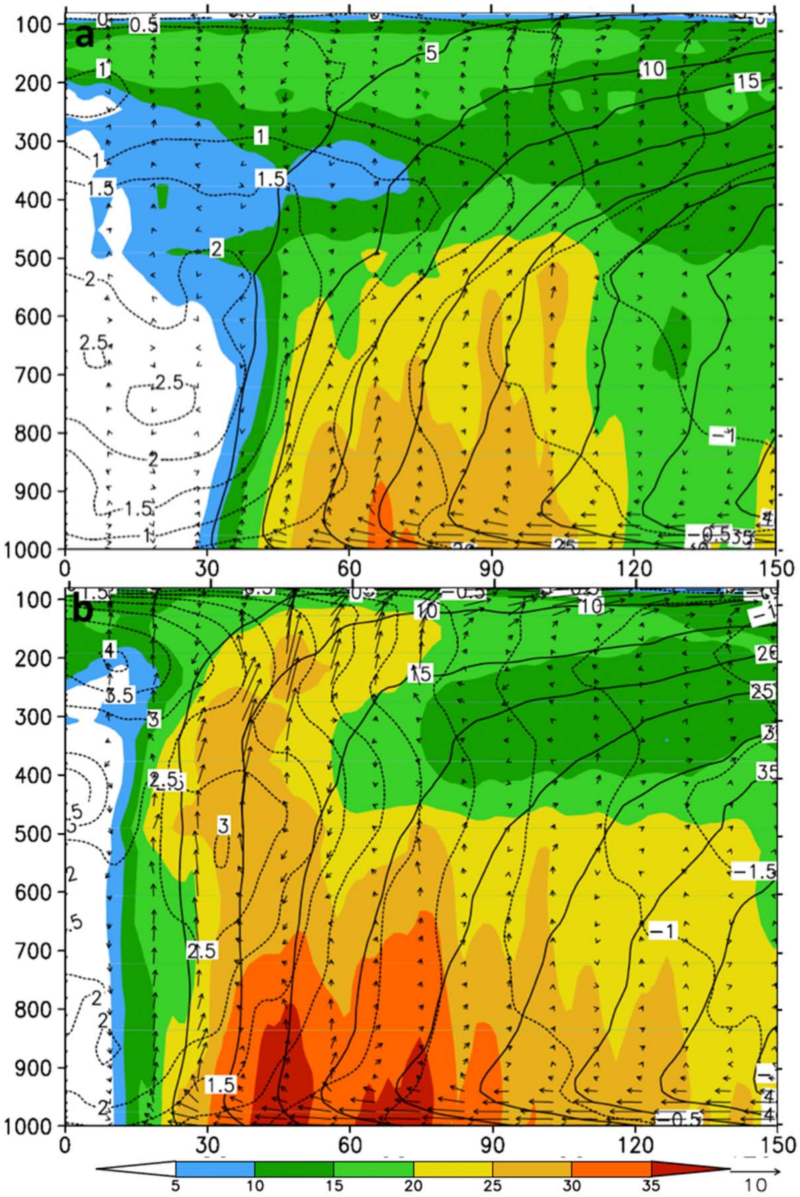

Figure 15. Vertical cross sections of the azimuthally averaged absolute angular momentum (solid, at intervals of 5×10^5 m^2 s^{-1}), potential temperature deviations (dashed, every 0.5°C), radar reflectivity (shaded) and in-plane flow vectors (m s^{-1}), from (a) 8/12–72, and (b) 9/12–96. Vertical motion has been multiplied by 10.

vertical axis of the radius of maximum wind (RMW) are nearly upright during the mature stage. Such upright structures could be examined using azimuthally averaged AAM maps, since the AAM is conserved following air parcels in the eyewall above the PBL [*Zhang et al.*, 2001]. It is apparent from Figure 15 that the AAM surfaces in the eyewall tilt outward prior to 8/12–72, and become nearly upright up to 250 hPa by 9/12–96, but still tilt outward in the outer regions. On the basis of the results shown in Figures 2 and 14, we may attribute the generation of the above mentioned upright structures to the presence of the midlevel convergent sheared flows, which is enhanced by convective heating aloft (Figure 15). Note the shift of the peak warm core from 750 to 200 hPa as the AAM surfaces become more upright from 8/12–72 to 9/12–96. This near-upright structure also explains why Nari looks more compact at later stages (see Figure 5). The simulated Nari is also more robust at this near-upright stage, with updrafts reaching as high as near 100 hPa (cf. Figures 14b and 14c).

[39] Finally, Figure 16 shows the time series of the mean vertical relative vorticity and the mean vortex stretching rates; vortex tilting rates are small under the present weak VWS environment. Apparently, the mean cyclonic vorticity grows with time, mostly in the lowest 200 hPa, except for the last few hours of the 4 day period, which is consistent with the simulated intensity variations given in Figure 6; this leads to the generation of the maximum rotation slightly below 900 hPa where the PBL top is located. The midlevel

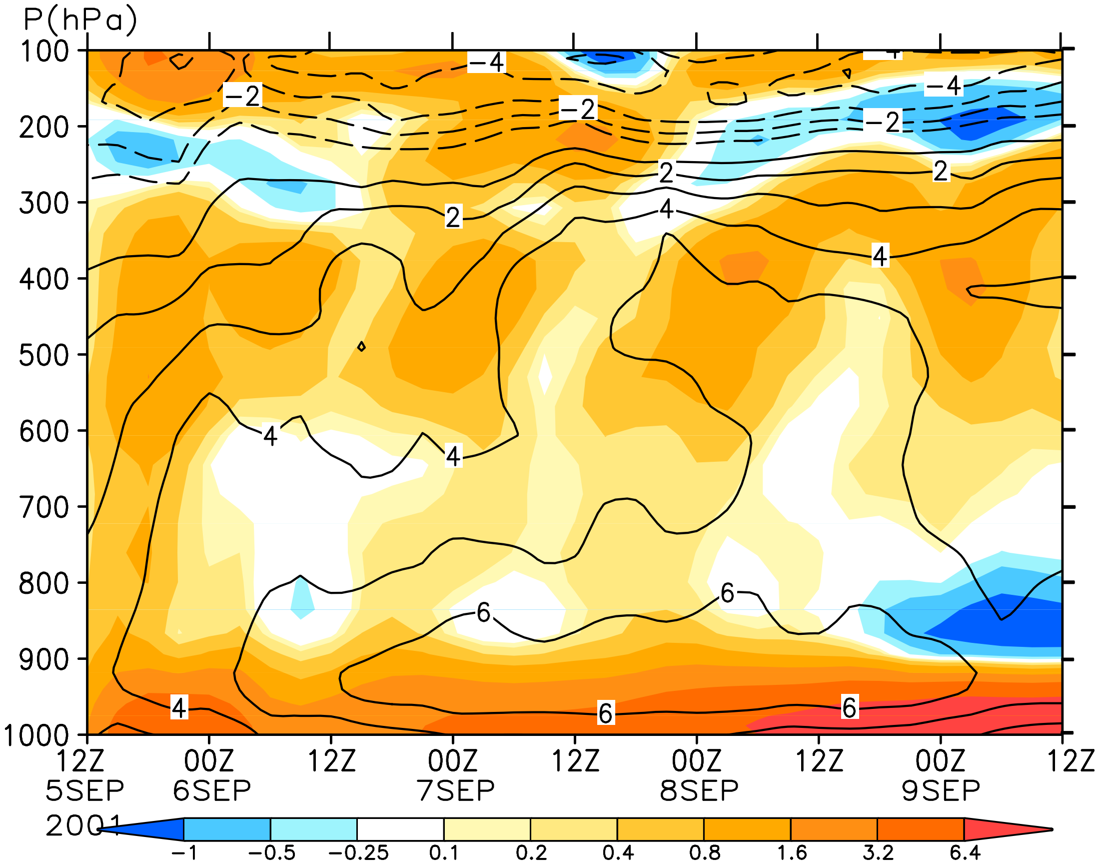

Figure 16. Height-time cross section of the area-averaged vertical relative vorticity (contoured, 10^{-5} s^{-1}), and the area-averaged stretching rates (color shaded, 10^{-9} s^{-2}) from the 96 h simulation, valid between 1200 UTC, 5 September, and 1200 UTC, 9 September 2001; they are obtained over an area of 800 km × 800 km centered at the surface circulation.

vorticity increases slightly during the same period. In contrast, the upper-level anticyclonic vorticity remains at nearly the same intensity, although the outflow layer thickness decreases slowly, which conforms with the higher penetration depth of deep convection at the mature stage (cf. Figures 14 and 16). Note that the vertical vorticity structures of Nari resemble closely those shown by *Zhang and Bao* [1996b, Figures 2 and 4] for a TCG event in a near-barotropic environment, but differ from those of Tropical Storm Eugene (2005) shown by *Kieu and Zhang* [2009, Figure 9], in which the peak cyclonic vorticity becomes elevated with time because of the development of extensive moist downdrafts.

[40] Of importance is that the vortex stretching rates are peaked at the surface where the frictional convergence is maximized (Figure 16) and that the net generation rates, consisting of both stretching and tilting, above the PBL are small because of the cancellation effects of tilting (not shown). (Clearly, the frictional dissipation accounts for the generation of weaker cyclonic vorticity in the PBL in the presence of the large stretching rates.) This implies that the TC-scale rotation is amplified near the PBL top via stretching of the absolute vorticity in the presence of intense convergence, and it is then advected by deep convection and mesoscale updrafts into the midtroposphere and upper troposphere during both TCG and subsequent intensification (Figures 14 and 16). Such a bottom-up process confirms that first shown by *Zhang and Bao* [1996a, 1996b] and later by *Hendricks et al.* [2004] as the likely mechanism for TCG.

[41] Significant vortex stretching is also evident in the 300–600 hPa layer, as also shown in Figure 14. Clearly, this accounts partly for the increased midlevel rotation of the typhoon vortex, making the constant vorticity and AAM surfaces at the vortex outer edge nearly upright (cf. Figures 14d, 15, and 16), as mentioned before.

6. Summary and Concluding Remarks

[42] In this study, we focused on the origin and genesis of Typhoon Nari (2001) and its early erratic looping track using the large-scale analysis, satellite observations, and a 4 day nested-grid, cloud-resolving simulation with the PSU-NCAR mesoscale (MM5) model at the finest grid size of 1.33 km. Observational analysis indicates that Nari could be traced more than 5 days back to a diurnally varying MCS/MCV in the tropical easterly flows, and it evolved under the influence of a subtropical high, an eastward-traveling midlatitude disturbance with a weak surface front, an approaching-and-departing Typhoon Danas to the east, and the Kuroshio Current.

[43] Results show that despite the use of the large-scale initial conditions, the MM5 could reproduce reasonably well

the genesis, final intensity, and looping track as well as the general convective activity of Nari during the 4 day period. In addition, the model captures two deep subvortices at the eye-eyewall interface that are similar in scale to those observed at a later stage, few spiral rainbands, and the midget storm size. The subvortices are also similar to those observed in other TCs, and they appear to play an important role during Nari's intensification. It is found that the passage of a weak surface front plays a role in distorting the MCV and suppressing the preexisting convection within the MCS during the period of 1200 UTC, 5 September to1200 UTC, 6 September. TCG is not initiated until after the complete passage of this baroclinic disturbance, when vertical wind shear is significantly reduced and the MCV circulation is fully recovered. It is the development of two asymmetric rainbands during the early intensifying stage that gives rise to the formation of a small eyewall from a preexisting larger vortex circulation, whereas the relatively dry and stable environment accounts for the development of few rainbands in the outer region and so the midget-sized storm.

[44] An analysis of the MM5 and earlier oceanic modeling results indicates that Fujiwhara's vortex-vortex interaction with Danas accounts for the looping track of the storm, while Nari's variable intensity changes during its looping stages are determined partly by its interaction with the Kuroshio Current [*Wu et al.*, 2008] and partly by the vortex-vortex interaction that appears to prevent it from accessing CAPE in its larger-scale environment. The MM5 under-predicts Nari's intensity as it moves across the Kuroshio because of the lack of the coupled air-sea interactive process. Our results confirm the previous finding of the bottom-up growth of cyclonic vorticity during TCG and subsequent intensification, with the peak rotation occurring near the top of the PBL. Results also show that the middle- to upper-level convergent flows associated with the subtropical high and Danas produce nearly upright vorticity and absolute angular momentum surfaces, leading to the generation of upright convection and RMW in the eyewall. This larger-scale convergence also helps increase the rotation and contraction of the storm in the midtroposphere.

[45] **Acknowledgments.** We wish to thank Chris Velden and Dave Stettner of the University of Wisconsin-Madison for providing the satellite imagery used in Figure 3 and Lin Zhu for plotting some of the figures used for this study. This work was supported by the Typhoon Research Project (2009CB421503) of the National Basic Research Program (the 973 Program) of China, ONR grant N000140710186, and NSF grant ATM0758609. MJY was supported by the National Science Council of Taiwan under grants NSC 99-2625-M-008-005-MY3 and 100-2119-M-008-017. The model integration was performed on the supercomputers of the National Center for Atmospheric Research, which is sponsored by the National Science Foundation.

References

Bartels, D. L., and R. A. Maddox (1991), Midlevel cyclonic vortices generated by mesoscale convective systems, *Mon. Weather Rev.*, *119*, 104–118, doi:10.1175/1520-0493(1991)119<0104:MCVGBM>2.0.CO;2.

Bosart, L. F., and F. Sanders (1981), The Johnstown flood of July 1977: A long-lived convective storm, *J. Atmos. Sci.*, *38*, 1616–1642, doi:10.1175/1520-0469(1981)038<1616:TJFOJA>2.0.CO;2.

Brandes, E. A. (1990), Evolution and structure of the 6–7 May 1985 mesoscale convective system and associated vortex, *Mon. Weather Rev.*, *118*, 109–127, doi:10.1175/1520-0493(1990)118<0109:EASOTM>2.0.CO;2.

Braun, S. A. (2002), A cloud-resolving simulation of Hurricane Bob (1991), storm structure and eyewall buoyancy, *Mon. Weather Rev.*, *130*, 1573–1592, doi:10.1175/1520-0493(2002)130<1573:ACRSOH>2.0.CO;2.

Davis, C. A., et al. (2004), The bow echo and MCV experiment: Observations and opportunities, *Bull. Am. Meteorol. Soc.*, *85*, 1075–1093, doi:10.1175/BAMS-85-8-1075.

Dudhia, J. (1993), A nonhydrostatic version of the Penn State–NCAR mesoscale model: Validation tests and simulation of an Atlantic cyclone and cold front, *Mon. Weather Rev.*, *121*, 1493–1513, doi:10.1175/1520-0493(1993)121<1493:ANVOTP>2.0.CO;2.

Dunkerton, T. J., M. T. Montgomery, and Z. Wang (2009), Tropical cyclogenesis in a tropical wave critical layer: Easterly waves, *Atmos. Chem. Phys.*, *9*, 5587–5646, doi:10.5194/acp-9-5587-2009.

Dvorak, V. F. (1984), Tropical cyclone intensity analysis using satellite data, *NOAA Tech. Rep. NESDIS 11*, 47 pp., NOAA, Silver Spring, Md.

Emanuel, K. A. (1986), An air-sea interaction theory for tropical cyclones. Part I: Steady-state maintenance, *J. Atmos. Sci.*, *43*, 585–605, doi:10.1175/1520-0469(1986)043<0585:AASITF>2.0.CO;2.

Fang, J., and F. Zhang (2010), Initial development and genesis of Hurricane Dolly (2008), *J. Atmos. Sci.*, *67*, 655–672, doi:10.1175/2009JAS3115.1.

Fujiwhara, S. (1921), The natural tendency towards symmetry of motion and its application as a principle in meteorology, *Q. J. R. Meteorol. Soc.*, *47*, 287–292, doi:10.1002/qj.49704720010.

Gamache, J. F., and R. A. Houze Jr. (1982), Mesoscale air motions associated with a tropical squall line, *Mon. Weather Rev.*, *110*, 118–135, doi:10.1175/1520-0493(1982)110<0118:MAMAWA>2.0.CO;2.

Gray, W., and R. W. Jacobson (1977), Diurnal variation of deep cumulus convection, *Mon. Weather Rev.*, *105*, 1171–1188, doi:10.1175/1520-0493(1977)105<1171:DVODCC>2.0.CO;2.

Halverson, J. B., et al. (2007), NASA's Tropical Cloud Systems and Processes (TCSP) Experiment: Investigating tropical cyclogenesis and hurricane intensity change, *Bull. Am. Meteorol. Soc.*, *88*, 867–882, doi:10.1175/BAMS-88-6-867.

Harr, P. A., and R. L. Elsberry (1996), Structure of a mesoscale convective system embedded in Typhoon Robyn during TCM-93, *Mon. Weather Rev.*, *124*, 634–652, doi:10.1175/1520-0493(1996)124<0634:SOAMCS>2.0.CO;2.

Harr, P. A., R. L. Elsberry, and J. C. L. Chan (1996), Transformation of a large monsoon depression to a tropical storm during TCM-93, *Mon. Weather Rev.*, *124*, 2625–2643, doi:10.1175/1520-0493(1996)124<2625:TOALMD>2.0.CO;2.

Haynes, P., and M. McIntyre (1987), On the evolution of vorticity and potential vorticity in the presence of diabatic heating and frictional or other forces, *J. Atmos. Sci.*, *44*, 828–841, doi:10.1175/1520-0469(1987)044<0828:OTEOVA>2.0.CO;2.

Hendricks, E. A., and M. T. Montgomery (2006), Rapid scan views of convectively generated mesovortices in sheared Tropical Cyclone Gustav (2002), *Weather Forecasting*, *21*, 1041–1050, doi:10.1175/WAF950.1.

Hendricks, E. A., M. T. Montgomery, and C. A. Davis (2004), The role of "vortical" hot towers in the formation of tropical cyclone Diana (1984), *J. Atmos. Sci.*, *61*, 1209–1232, doi:10.1175/1520-0469(2004)061<1209:TROVHT>2.0.CO;2.

Hill, K. A., and G. M. Lackmann (2009), Influence of environmental humidity on tropical cyclone size, *Mon. Weather Rev.*, *137*, 3294–3315, doi:10.1175/2009MWR2679.1.

Hogsett, W., and D.-L. Zhang (2010), Genesis of Typhoon Chanchu (2006) from a westerly wind burst associated with the MJO. Part I: Synoptic evolution of a tilted precursor vortex, *J. Atmos. Sci.*, *67*, 3774–3792, doi:10.1175/2010JAS3446.1.

Huo, Z.-H., D.-L. Zhang, and J. Gyakum (1999), The interaction of potential vorticity anomalies in extratropical cyclogenesis. Part I: Static piecewise inversion, *Mon. Weather Rev.*, *127*, 2546–2562, doi:10.1175/1520-0493(1999)127<2546:IOPVAI>2.0.CO;2.

Janowiak, J. E., P. A. Arkin, and M. Morrissey (1994), An examination of the diurnal cycle in oceanic tropical rainfall using satellite and in situ data, *Mon. Weather Rev.*, *122*, 2296–2311, doi:10.1175/1520-0493(1994)122<2296:AEOTDC>2.0.CO;2.

Kain, J. S. (2004), The Kain-Fritsh convective parameterization: An update, *J. Appl. Meteorol.*, *43*, 170–181, doi:10.1175/1520-0450(2004)043<0170:TKCPAU>2.0.CO;2.

Kieu, C. Q., and D.-L. Zhang (2008), Genesis of Tropical Storm Eugene (2005) from merging vortices associated with ITCZ breakdowns, Part I: Observational and modelling analyses, *J. Atmos. Sci.*, *65*, 3419–3439, doi:10.1175/2008JAS2605.1.

Kieu, C. Q., and D.-L. Zhang (2009), Genesis of Tropical Storm Eugene (2005) from merging vortices associated with ITCZ breakdowns, Part II: Roles of vortex merger and ambient potential vorticity, *J. Atmos. Sci.*, *66*, 1980–1996, doi:10.1175/2008JAS2905.1.

Kossin, J. P., B. D. McNoldy, and W. H. Schubert (2002), Vortical swirls in hurricane eye clouds, *Mon. Weather Rev.*, *130*, 3144–3149, doi:10.1175/1520-0493(2002)130<3144:VSIHEC>2.0.CO;2.

Kurihara, Y., and R. E. Tuleya (1981), A numerical simulation study on the genesis of a tropical storm, *Mon. Weather Rev.*, *109*, 1629–1653, doi:10.1175/1520-0493(1981)109<1629:ANSSOT>2.0.CO;2.

Lander, M. A. (1990), Evolution of the cloud pattern during the formation of tropical cyclone twins symmetrical with respect to the equator, *Mon. Weather Rev.*, *118*, 1194–1202, doi:10.1175/1520-0493(1990)118<1194:EOTCPD>2.0.CO;2.

Lander, M. A. (1994), Description of a monsoon gyre and its effects on the tropical cyclones in the western North Pacific during August 1991, *Weather Forecasting*, *9*, 640–654, doi:10.1175/1520-0434(1994)009<0640:DOAMGA>2.0.CO;2.

Leary, C. A., and E. N. Rappaport (1987), The life cycle and internal structure of a mesoscale convective complex, *Mon. Weather Rev.*, *115*, 1503–1527, doi:10.1175/1520-0493(1987)115<1503:TLCAIS>2.0.CO;2.

Liu, Y., D.-L. Zhang, and M. K. Yau (1997), A multiscale numerical study of Hurricane Andrew (1992). Part I: Explicit simulation and verification, *Mon. Weather Rev.*, *125*, 3073–3093, doi:10.1175/1520-0493(1997)125<3073:AMNSOH>2.0.CO;2.

Liu, Y., D.-L. Zhang, and M. K. Yau (1999), A multiscale numerical study of Hurricane Andrew (1992). Part II: Kinematics and inner-core structures, *Mon. Weather Rev.*, *127*, 2597–2616, doi:10.1175/1520-0493(1999)127<2597:AMNSOH>2.0.CO;2.

Molinari, J., D. Vollaro, D. S. Skubis, and M. Dickinson (2000), Origins and mechanisms of Eastern Pacific tropical cyclogenesis: A case study, *Mon. Weather Rev.*, *128*, 125–139, doi:10.1175/1520-0493(2000)128<0125:OAMOEP>2.0.CO;2.

Montgomery, M. T., et al. (2011), The pre-depression investigation of cloud systems in the tropics (PREDICT) experiment: Scientific basis, new analysis tools, and some first results, *Bull. Am. Meteor. Soc.*, doi:10.1175/BAMS-D-11-00046.1, in press.

Montgomery, M. T., M. E. Nicholls, T. A. Cram, and A. B. Saunders (2006), A vortical hot tower route to tropical cyclogenesis, *J. Atmos. Sci.*, *63*, 355–386, doi:10.1175/JAS3604.1.

Montgomery, M. T., N. V. Sang, R. K. Smith, and J. Persing (2009), Do tropical cyclones intensify by WISHE?, *Q. J. R. Meteorol. Soc.*, *135*, 1697–1714, doi:10.1002/qj.459.

Nolan, D. S. (2007), What is the trigger for tropical cyclogenesis?, *Aust. Meteorol. Mag.*, *56*, 241–266.

Ogura, Y., and M.-T. Liou (1980), The structure of a midlatitude squall line, *J. Atmos. Sci.*, *37*, 553–567, doi:10.1175/1520-0469(1980)037<0553:TSOAMS>2.0.CO;2.

Reasor, P. D., M. T. Montgomery, and L. F. Bosart (2005), Mesoscale observations of the genesis of Hurricane Dolly (1996), *J. Atmos. Sci.*, *62*, 3151–3171, doi:10.1175/JAS3540.1.

Ritchie, E. A., and G. J. Holland (1997), Scale interactions during the formation of Typhoon Irving, *Mon. Weather Rev.*, *125*, 1377–1396, doi:10.1175/1520-0493(1997)125<1377:SIDTFO>2.0.CO;2.

Ritchie, E. A., and G. J. Holland (1999), Large-scale patterns associated with tropical cyclogenesis in the western Pacific, *Mon. Weather Rev.*, *127*, 2027–2043, doi:10.1175/1520-0493(1999)127<2027:LSPAWT>2.0.CO;2.

Rogers, R. F., S. S. Chen, J. E. Tenerelli, and H. Willoughby (2003), A numerical study of the impact of vertical shear on the distribution of rainfall in Hurricane Bonnie (1998), *Mon. Weather Rev.*, *131*, 1577–1599, doi:10.1175//2546.1.

Schubert, W. H., M. T. Montgomery, R. K. Taft, T. A. Guinn, S. R. Fulton, J. P. Kossin, and J. P. Edwards (1999), Polygonal eyewalls, asymmetric eye contraction, and potential vorticity mixing in hurricanes, *J. Atmos. Sci.*, *56*, 1197–1223, doi:10.1175/1520-0469(1999)056<1197:PEAECA>2.0.CO;2.

Tang, B., and K. Emanuel (2010), Midlevel ventilation's constraint on tropical cyclone intensity, *J. Atmos. Sci.*, *67*, 1817–1830, doi:10.1175/2010JAS3318.1.

Tao, W.-K., and J. Simpson (1993), The Goddard cumulus ensemble model. Part I: Model description, *Terr. Atmos. Oceanic Sci.*, *4*, 35–72.

Verlinde, J., and W. R. Cotton (1990), A mesovortex couplet in the trailing anvil region of a multicellular convective complex, *Mon. Weather Rev.*, *118*, 993–1010, doi:10.1175/1520-0493(1990)118<0993:AMVCOI>2.0.CO;2.

Wang, C.-C., and G. Magnusdottir (2006), The ITCZ in the central and Eastern Pacific on synoptic time scales, *Mon. Weather Rev.*, *134*, 1405–1421, doi:10.1175/MWR3130.1.

Wang, Z., M. T. Montgomery, and T. J. Dunkerton (2010), Genesis of pre–Hurricane Felix (2007). Part I: The role of the easterly wave critical layer, *J. Atmos. Sci.*, *67*, 1711–1729, doi:10.1175/2009JAS3420.1.

Wu, L., S. A. Braun, J. Halverson, and G. Heymsfield (2006), A numerical study of Hurricane Erin (2001). Part I: Model verification and storm evolution, *J. Atmos. Sci.*, *63*, 65–86, doi:10.1175/JAS3597.1.

Wu, C.-R., Y.-L. Chang, L.-Y. Oey, C.-W. J. Chang, and Y.-C. Hsin (2008), Air-sea interaction between tropical cyclone Nari and Kuroshio, *Geophys. Res. Lett.*, *35*, L12605, doi:10.1029/2008GL033942.

Yang, M.-J., D.-L. Zhang, and H.-L. Huang (2008), A modeling study of Typhoon Nari (2001) at landfall. Part I: Topographic effects, *J. Atmos. Sci.*, *65*, 3095–3115, doi:10.1175/2008JAS2453.1.

Yang, M.-J., D.-L. Zhang, X.-D. Tang, and Y. Zhang (2011), A modeling study of Typhoon Nari (2001) at landfall. 2: Structure changes and terrain-induced asymmetries, *J. Geophys. Res.*, *116*, D09112, doi:10.1029/2010JD015445.

Zhang, D.-L. (1992), The formation of a cooling-induced mesovortex in the trailing stratiform region of a midlatitude squall line, *Mon. Weather Rev.*, *120*, 2763–2785, doi:10.1175/1520-0493(1992)120<2763:TFOACI>2.0.CO;2.

Zhang, D.-L., and R. A. Anthes (1982), A high-resolution model of the planetary boundary layer —Sensitivity tests and comparisons with SESAME-79 data, *J. Appl. Meteorol.*, *21*, 1594–1609, doi:10.1175/1520-0450(1982)021<1594:AHRMOT>2.0.CO;2.

Zhang, D.-L., and N. Bao (1996a), Oceanic cyclogenesis as induced by a mesoscale convective system moving offshore. Part I: A 90-h real-data simulation, *Mon. Weather Rev.*, *124*, 1449–1469, doi:10.1175/1520-0493(1996)124<1449:OCAIBA>2.0.CO;2.

Zhang, D.-L., and N. Bao (1996b), Oceanic cyclogenesis as induced by a mesoscale convective system moving offshore. Part II: Genesis and thermodynamic transformation, *Mon. Weather Rev.*, *124*, 2206–2226, doi:10.1175/1520-0493(1996)124<2206:OCAIBA>2.0.CO;2.

Zhang, D.-L., and J. M. Fritsch (1987), Numerical simulation of the meso-β-scale structure and evolution of the 1977 Johnstown flood. Part II: Inertially stable warm-core vortex and the mesoscale convective complex, *J. Atmos. Sci.*, *44*, 2593–2612, doi:10.1175/1520-0469(1987)044<2593:NSOTMS>2.0.CO;2.

Zhang, D.-L., and J. M. Fritsch (1988), A numerical investigation of a convectively generated, inertially stable, extratropical warm-core mesovortex over land. Part I: Structure and evolution, *Mon. Weather Rev.*, *116*, 2660–2687, doi:10.1175/1520-0493(1988)116<2660:ANIOAC>2.0.CO;2.

Zhang, D.-L., H.-R. Chang, N. L. Seaman, T. T. Warner, and J. M. Fritsch (1986), A two-way interactive nesting procedure with variable terrain resolution, *Mon. Weather Rev.*, *114*, 1330–1339, doi:10.1175/1520-0493(1986)114<1330:ATWINP>2.0.CO;2.

Zhang, D.-L., Y. Liu, and M. K. Yau (2001), A multiscale numerical study of Hurricane Andrew (1992). Part IV: Unbalanced flows, *Mon. Weather Rev.*, *129*, 92–107, doi:10.1175/1520-0493(2001)129<0092:AMNSOH>2.0.CO;2.

Zhu, T., D.-L. Zhang, and F. Weng (2004), Numerical simulation of Hurricane Bonnie (1998). Part I: Eyewall evolution and intensity changes, *Mon. Weather Rev.*, *132*, 225–241, doi:10.1175/1520-0493(2004)132<0225:NSOHBP>2.0.CO;2.

Zipser, E. J., et al. (2009), The Saharan air layer and the fate of African easterly waves: NASA's AMMA 2006 field program to study tropical cyclogenesis, *Bull. Am. Meteorol. Soc.*, *90*, 1137–1156, doi:10.1175/2009BAMS2728.1.

L. Tian, Hebei Meteorological Observatory, 178 Tiyu St., Shijiazhuang, Hebei 050021, China.

M.-J. Yang, Department of Atmospheric Sciences, Institute of Hydrological and Oceanic Sciences, National Central University, 300 Chung-Da Rd., Chung-Li 320, Taiwan.

D.-L. Zhang, Department of Atmospheric and Oceanic Science, University of Maryland, College Park, MD 20742-2425, USA. (dalin@atmos.umd.edu)